SANDIA REPORT
SAND2012-8195
Unlimited Release
September 2012

From Benchtop to Raceway: Spectroscopic Signatures of Dynamic Biological Processes in Algal Communities

Jerilyn A. Timlin, Howland D.T. Jones, Thomas A. Reichardt, David T. Hanson, Amy J. Powell, Scott C. James, Patricia E. Gharagozloo, Aaron M. Collins, Anne Ruffing, Kylea Parchert, Brian P. Dwyer, Omar F. Garcia, Thomas A. Dempster, John A. McGowen, Christine Trahan, John Roesgen, Samuel Lopez-Nieves, Vijay Janardhanam, Varun Boriah, Andrew August, Kurt Sansom

Prepared by
Sandia National Laboratories
Albuquerque, New Mexico 87185 and Livermore, California 94550

Sandia National Laboratories is a multi-program laboratory managed and operated by Sandia Corporation, a wholly owned subsidiary of Lockheed Martin Corporation, for the U.S. Department of Energy's National Nuclear Security Administration under contract DE-AC04-94AL85000.

Approved for public release; further dissemination unlimited.

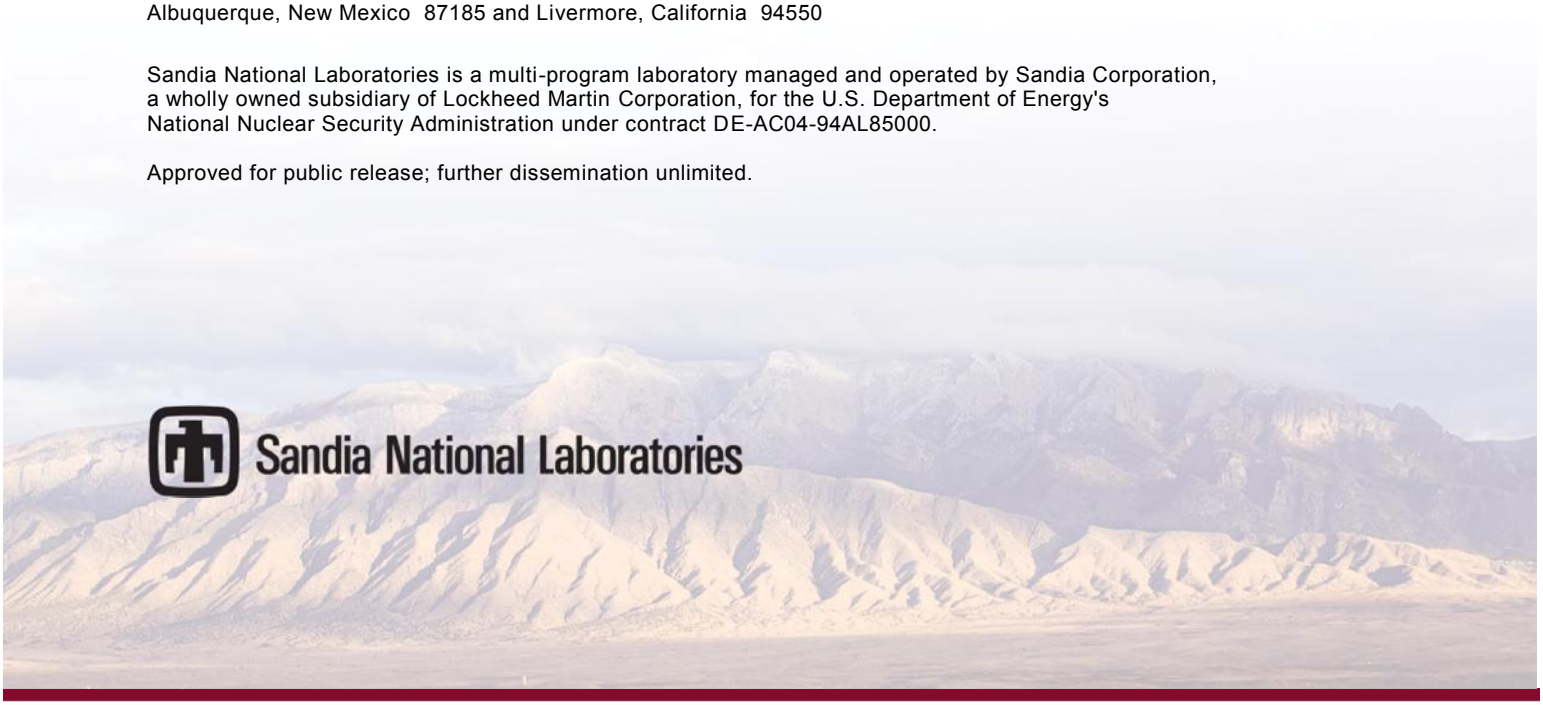

Issued by Sandia National Laboratories, operated for the United States Department of Energy by Sandia Corporation.

NOTICE: This report was prepared as an account of work sponsored by an agency of the United States Government. Neither the United States Government, nor any agency thereof, nor any of their employees, nor any of their contractors, subcontractors, or their employees, make any warranty, express or implied, or assume any legal liability or responsibility for the accuracy, completeness, or usefulness of any information, apparatus, product, or process disclosed, or represent that its use would not infringe privately owned rights. Reference herein to any specific commercial product, process, or service by trade name, trademark, manufacturer, or otherwise, does not necessarily constitute or imply its endorsement, recommendation, or favoring by the United States Government, any agency thereof, or any of their contractors or subcontractors. The views and opinions expressed herein do not necessarily state or reflect those of the United States Government, any agency thereof, or any of their contractors.

Printed in the United States of America. This report has been reproduced directly from the best available copy.

Available to DOE and DOE contractors from
U.S. Department of Energy
Office of Scientific and Technical Information
P.O. Box 62
Oak Ridge, TN 37831

Telephone: (865) 576-8401
Facsimile: (865) 576-5728
E-Mail: reports@adonis.osti.gov
Online ordering: http://www.osti.gov/bridge

Available to the public from
U.S. Department of Commerce
National Technical Information Service
5285 Port Royal Rd.
Springfield, VA 22161

Telephone: (800) 553-6847
Facsimile: (703) 605-6900
E-Mail: orders@ntis.fedworld.gov
Online order: http://www.ntis.gov/help/ordermethods.asp?loc=7-4-0#online

SAND2012-8195
Unlimited Release
September 2012

From Benchtop to Raceway: Spectroscopic Signatures of Dynamic Biological Processes in Algal Communities

Jerilyn A. Timlin, Howland D.T. Jones, Aaron M. Collins, Anne Ruffing, Kylea Parchert, Christine Trahan, Omar F. Garcia
Bioenergy and Defense Technologies

Amy J. Powell
Nanobiology

Brian P. Dwyer
Geotechnology & Engineering

Sandia National Laboratories
P.O. Box 5800
Albuquerque, New Mexico 87185-MS0895

Thomas A. Reichardt
Remote Sensing and Energetic Materials

Scott C. James, Patricia E. Gharagozloo, Varun Boriah, Andrew August, Kurt Sansom
Thermal/Fluid Science and Engineering

Sandia National Laboratories
P.O. Box 5800
Livermore, CA

David T. Hanson, Vijay Janardhanam, John Roesgen, Samuel Lopez-Nieves
Department of Biology
University of New Mexico
Albuquerque, New Mexico 87131

Thomas A. Dempster, John A. McGowen
Arizona Center for Algae Technology and Innovation
Arizona State University
Mesa, AZ 85212

Abstract

Major scientific challenges hinder the success of an industrial-scale algal biofuels program. Four broad areas of R&D needs have been identified for economically viable, industrial-scale cultivation of algae: culture sustainability; system productivity; nutrient source scaling and sustainability; and water conservation, management, and recycling. Progress in each of these areas is limited by significant knowledge gaps in fundamental algal biology. This SAND report summarizes research conducted as part of an LDRD project (FY10- FY12) to address this shortcoming. We have developed a novel, multidisciplinary, multiscale approach utilizing Sandia's core expertise in bioanalytical spectroscopy, chemical imaging, remote sensing, genomics, and computational modeling in collaboration with researchers at University of New Mexico and Arizona State University to investigate the effects that dynamic abiotic and biotic stressors have on algal photosynthesis, growth, and lipid production. The discoveries will enable gains in productivity and sustainability that are critical for cost-effective, industrial-scale algal facilities.

ACKNOWLEDGMENTS

The authors of this SAND report acknowledge the following people who provided additional assistance to enable the success of the project:

Jesse Aaron – *microscopy training for student interns*

Kathy Alam, Laura Martin – *scatter-free absorbance measurements*

Thomas Beechem, Anthony McDonald – *assistance with Raman microscopy*

Laura Carney, Todd Lane, Owen Solberg – *sequencing support*

Bryan Carson, Darren Branch – *use of laboratories and equipment*

Randy Edwards --- *administrative support*

Lindsey Gloe – *laboratory assistance*

Maureen Kessler, Michelle Raymer – *experimental support*

Sadie La Bueve – *assistance in qPCR protocols*

Pete Lammers (NMSU) – *early discussions leading to idea formulation*

Qiang Hu, Danxiang (May) Han (ASU) – *samples and expertise related to the Raman microscopy of Haematococcus.*

Grant Heffelfinger, Anthony Martino, Ron Pate, Blake Simmons, Ben Wu – *program development*

Lucas McGrath – *assistance with greenhouse equipment and infrastructure*

Charlotte Mobarak – *testing MALDI-TOF methods for measuring lipid composition*

Jackie Murton, Bryce Ricken – *experimental support in early phases of the project*

Randal Schmitt – *calibration of bulk sample laser-induced fluorescence measurements.*

Michael Sinclair – *hyperspectral imaging support, two-photon excitation alignment and acquisition*

Becky Bixby, Steve Scholle, and Tom Turner (UNM) – *assistance with algal pigment and community composition analyses*

David Van Horn (UNM) – *kind loan of sensors for greenhouse studies*

Rachel Zulick – *assistance with culture maintenance at UNM*

CONTENTS

NOMENCLATURE

A thaliana	*Arabidopsis thaliana*
ASU	Arizona State University
AzCATI	Arizona Center for Algae Technology and Innovation
CCM	carbon concentrating mechanism
C. reinhardtii	*Chlamydomonas reinhardtii*
cDNA	complementary deoxyribonucleic acid
DCW	Dry cell weight
DMSO	dimethyl sulfoxide
DNA	deoxyribonucleic acid
DOE	Department of Energy
gDNA	genomic deoxyribonucleic acid
H_2DCFDA	2,7-dichloro fluorescein diacetate
LDRD	Laboratory Directed Research and Development
LHCII	Light harvesting complex II
ly	Langly
MCR	Multivariate curve resolution
N. gaditana	*Nannochloropsis gaditana*
N. salina	*Nannochloropsis salina*
NaCl	Sodium chloride
NCGR	National Center for Genome Resources
PAM	Pulse amplitude modulated
PCD	Programmed cell death
PPM	Parts per million
PSI	Photosystem I
PSII	Photosystem II
qRT-PCR	Quantitative real-time polymerase chain reaction
RNA	ribonucleic acid
ROS	Reactive oxygen species
SNL	Sandia National Laboratories
TAP	tris-acetate-phosphate
UNM	University of New Mexico

1. INTRODUCTION

This SAND report summarizes research conducted as part of an LDRD project funded from October 1, 2009 through September 30, 2012

1.1. Background and Motivation

Microalgae can accumulate large amounts of oil (triacylglycerols) and polar lipids that can be converted to biodiesel and JP8 aviation fuel with currently available technology. Algae have many advantages including an inherently high photosynthetic efficiency, ability to utilize CO_2 and potentially reduce greenhouse gas emissions, and they will not compete with food production. Together these properties make microalgae an important potential piece in the renewable energy puzzle. However, like lignocellulosic materials, there are major scientific challenges to an industrial-scale algal biofuels program. Recently, four broad areas of R&D needs have been identified for economically viable, industrial-scale cultivation of algae: culture sustainability; system productivity; nutrient source scaling and sustainability; and water conservation, management, and recycling. Progress in each of these areas is limited by significant knowledge gaps in fundamental algal biology specifically surrounding the response of microalagae to dynamic environmental parameters.

To quote the Algal Biofuels Roadmap: "Methods for automated biological and chemical monitoring in production settings will be essential for assessing the health and compositional dynamics of algal ponds." To achieve this, a tool kit including sensitive, selective methods for the early detection of fluctuations in algal health, productivity, and invasive algal strains, pathogens and predators must be developed. At present very little is known about the effect these changes have on the biochemical indicators of algae health. Data are particularly scarce for locations in the southwestern U.S. that have the land, sunlight and saltwater resources required for large scale algal cultivation. In summary, these facts make our proposed research important, timely, and relevant not only on the DOE's mission for sustainable, affordable energy, but also right here in our backyard.

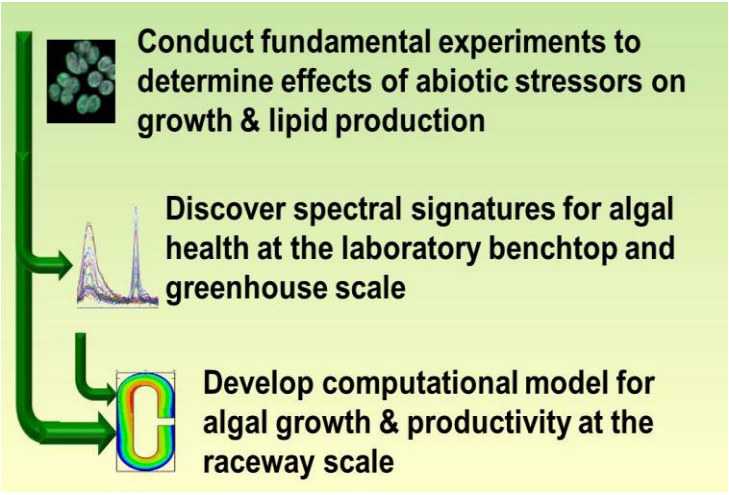

Figure 1-1: The primary goals of the project with arrows to highlight the strong integration across the different disciplines.

1.2. Technical Approach

This project begins to address the knowledge gaps presented in Section 1.1. through the development and application of an innovative, multidisciplinary approach that combines traditional algal physiology with molecular biology, bioanalytical spectroscopy, chemical imaging,

remote sensing, transcriptomics, and computational modeling to pr ovide an improved fundamental understanding of algal growth and development. This permits identification of molecular and spectral biomarkers that indicate algal response to changing environmental conditions, translation of those biomarkers to field-based measurements, and development of a computational model capable of predicting algal growth at the industrial scale.

This approach has three main differentiating features, namely the emphasis on: a high- degree of integration (Figure 1.1), research over multiple spatial scales (Figure 1.2), and production-relevant, fundamental science.

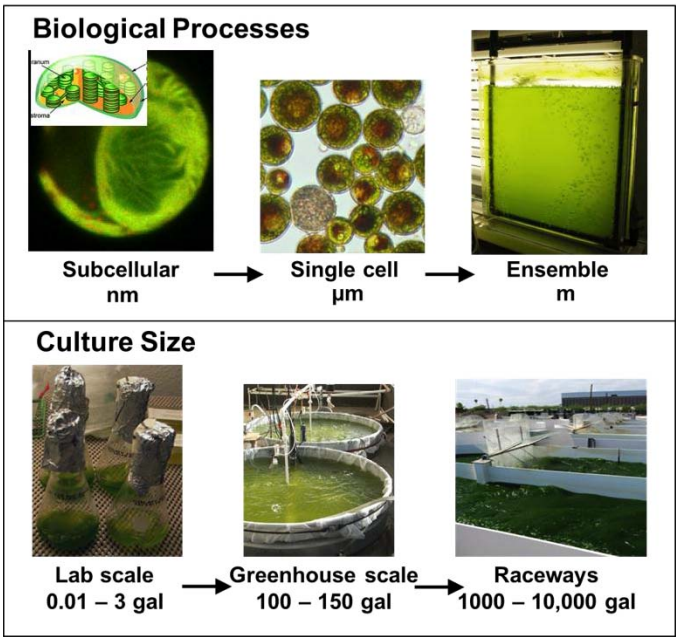

Figure 1-2: Investigations span multiple spatial scales in the biological processes studied as well as the culture size.

To ensure the project scope is manageable yet relevant the experiments utilize the model green alga *Chlamydomonas reinhardtii* (*C. reinhardtii*) as well as potential production strains of microalgae, including *Nannochloropsis salina (N. salina),* under optimal and CO_2 and salt stressed conditions.

1.3. Impact

This work fills a strategic niche in an important, yet largely unexplored area of biofuels where SNL has unique capabilities. The development of an integrated bioanalytical toolkit to provide sensitive, selective methods for detecting early fluctuations in algal health and productivity has the broad impact on algal biofuels and bioenergy, permitting early intervention and higher biomass production. This is aligned with the mission of Sandia National Laboratories in bioenergy and is directly relevant to the current national security mission of the Department of Energy.

This project has positively impacted Sandia National Laboratories algal biofuels program in four overarching areas: 1) growing the infrastructure, 2) developing differentiating technical capabilities, 3) using these capabilities to facilitate discoveries in algal biology, and 4) increasing our external visibility. These are detailed below.

Growing Algal Biology at the SNL-NM site:

- Development of a fully functional biological laboratory for culturing, manipulating, and conducting experiments on a variety of algae, cyanobacteria, fungi, viruses, and bacteria
- Ownership and maintenance of algal greenhouse facility

- Support of key hires in bioenergy/biofuels
- Support of a total of 5 student interns
- Development of key collaborations with Arizona State University, University of New Mexico, and Sapphire Energy

Developing Differentiating Technical Capabilities

- Development of hyperspectral reflectivity technology to remotely sense algal growth at the benchtop, greenhouse, and raceway scales.
- Development of multidimensional bioanalytical pipeline for conducting experiments at the laboratory and greenhouse scales.
- Discovery of spectroscopic signatures correlated to culture growth and productivity at laboratory and greenhouse scales and demonstrated the success of these methods at the industrial raceway scale.
- Development of predictive computational models of algal growth and productivity at the industrial scale.

Novel Biological Discoveries enabled by our Differentiating Capabilities

- Understanding of the effect of CO_2 stress on photosynthesis and lipid production in *N. salina*
- Real-time spectroscopic modeling of *N. salina* growth and stress in greenhouse
- Clarification of the boundary between stress and possible programmed cell death-like response in *C. reinhardtii* cells under salt stress

Increasing External Visibility

- Development of preliminary data and expertise for multiple internal and external proposal ideas
- 16 posters, 14 presentations at conferences (over ½ were invited)
- Publication of manuscripts in Algal Research, PlosONE, J. Computational Biology, J. Chemometrics & Intell Lab Systems.

Note: This SAND report is not meant to provide a comprehensive review of all of the experiments in elaborate detail, but rather capture the important highlights. Select experiments conducted and results generated as part of this LDRD project are described in the sections that follow. For detailed reports of the work conducted under this LDRD, the reader is referred to the peer-reviewed publications in print, press, and preparation. (Collins, 2011; James, 2010; Jones, 2012; Reichardt, 2012)

2. DEVELOPMENT OF HYPERSPECTRAL REFLECTIVITY FOR ASSESSING ALGAL GROWTH AND PRODUCTIVITY AT THE LABORATORY, GREENHOUSE, AND RACEWAY SCALES

2.1. Introduction

Both active and passive approaches can be considered for remote sensing of algal biofuel production. Whether applying an active or passive approach, the goal is to remotely assess the inherent optical properties (Baker, 1982) of the algal culture via the collection and interpretation of light from the sample. Both categories of approach rely on three processes – absorption, scattering, and fluorescence – to provide a spectral signature indicative of the culture constituents. While active approaches require transmission of light to the culture, typically in the form of a laser beam (Hoge, 2005), passive approaches rely instead on external lighting conditions (e.g., laboratory growth lamps or the sun) to provide the incident light. After performing initial demonstrations of both active and passive sensing at the laboratory benchtop scale, follow-on efforts focused on applying passive hyperspectral sensing to the greenhouse- and raceway-scales.

2.2. Laboratory Measurements

The laboratory measurements have been fully described in a recent publication (Reichardt, 2012), so only a brief summary is presented here. The laboratory reflectance instrument consisted of a dual-channel fiber-coupled spectroradiometer (Ocean Optics Jaz system). To capture the upwelling light, one channel of the spectroradiometer was connected to a bare fiber directed downward over a beaker containing the algal culture. The other channel was connected to a fiber with a cosine-corrector diffuser attachment directed upward to measure the downwelling light. The 0.22-numerical aperture (NA) of the bare fiber defined a $2\times\sin^{-1}(0.22) = 25^{o}$ field-of-view (FOV) for the downward-looking fiber, while the cosine corrector attached to the upward-looking fiber allowed for the full collection of downwelling light. The relative spectral responses of both channels were determined with an Ocean Optics LS-1 tungsten-halogen calibrated light source. Analysis of the resulting reflectance spectra (Reichardt, 2012) demonstrated successful extraction of the pigment optical activity and algal cell backscatter.

2.3. Greenhouse Measurements

Reflectance measurements were performed on two greenhouse-contained mini-ponds (6-ft diameter stock tanks) located in TAIII at Sandia NM (Figure 2-1). Each pond possesses a center-pivot with multiple arms for injecting air and carbon dioxide. The major challenge associated with acquiring reflectance measurements from these ponds resulted from the greenhouse itself: the structure casted shadows (Figure 2-2) onto the downwelling detector as well as into the FOV of the upwelling detector. In an attempt to reduce the impact of shadows on the acquired data, the downwelling detector was positioned within the FOV of the upwelling detector, with the goal of arranging the sensors to be more equally affected by the shadows. However, even in this configuration, the temporally varying shadows had an adverse effect on the reflectance spectra. Other challenges included stabilizing the temperature of the

spectroradiometer: the heat transfer capacity of the instrument enclosure, which utilized thermoelectric cooling, was sometimes insufficient for temperature stabilization.

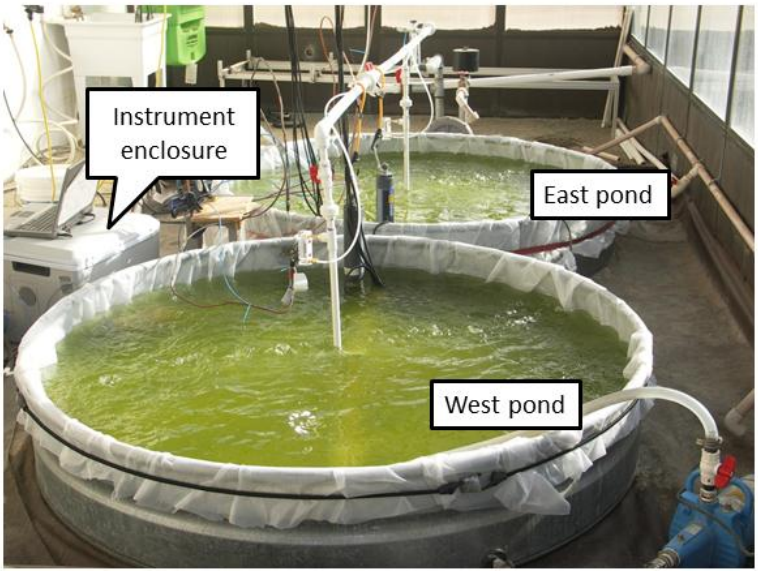

Figure 2-1. Mini-ponds in the Sandia greenhouse. Two dual-channel spectroradiometers were configured in the instrument enclosure that is positioned between the ponds.

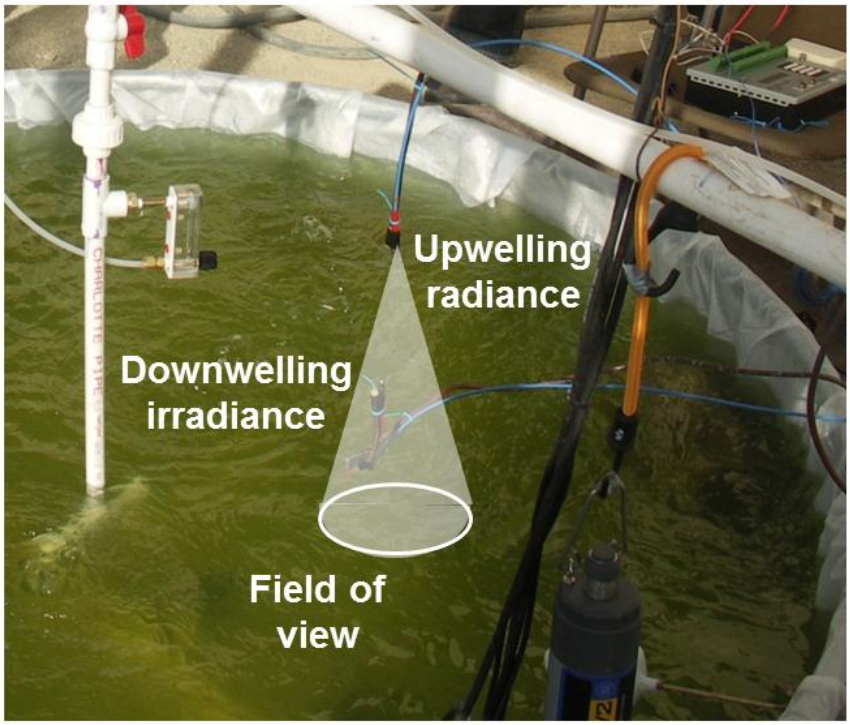

Figure 2-2. Reflectance measurement on mini-pond. The shadows cast by the greenhouse structure, evident especially in the right side of the photograph, varied throughout the day.

2.4. Raceway Demonstration

From July-September 2012, the reflectance-measurement instrument was deployed at the Arizona Center for Algae Technology and Innovation (AzCATI), located at Arizona State University's (ASU's) Polytechnic Campus in Mesa, AZ. (Figure 2-3) Measurements were conducted on a single raceway pond. C ompared to the laboratory and greenhouse measurements, two additional channels were added: (1) a bare fiber staring at zenith to collect the radiance directly overhead, and (2) a fiber submerged into the water to measure the below-surface radiance. The instrument temperature stabilization was upgraded to the use of an outdoor refrigerated enclosure (Summit SPR6OS 24) coupled to a digital thermostat control unit (Johnson Controls A419).

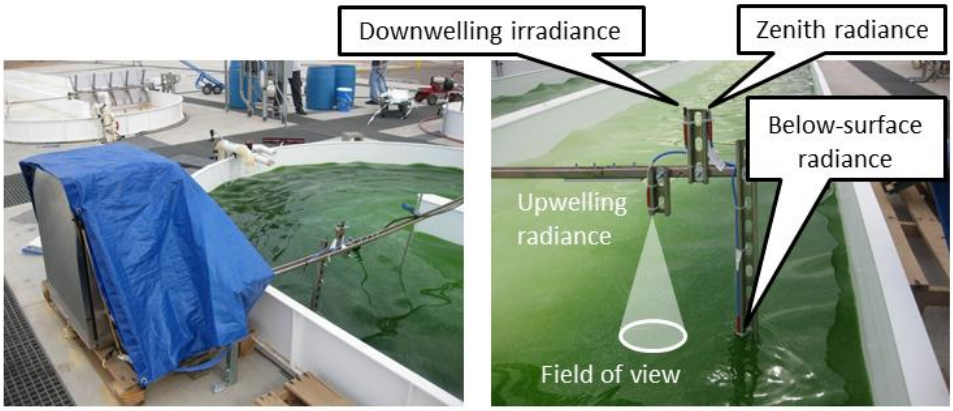

Figure 2-3 Reflectance measurement on the outdoor raceway pond at AzCATI.

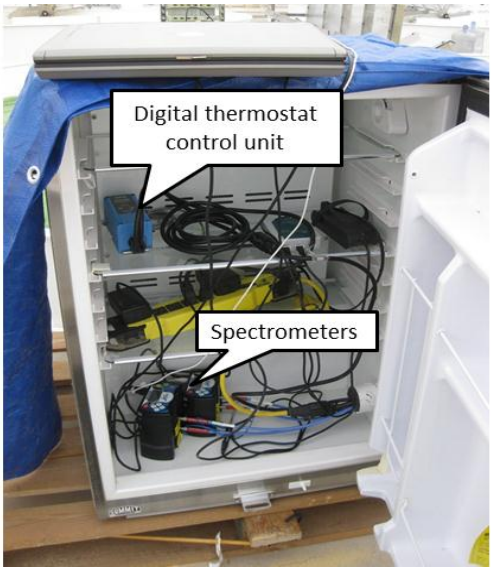

Figure 2-4 Spectroradiometer instrument configured inside temperature-controlled enclosure.

Reflectance spectra were acquired over the entire 12-day time span of *N. salina* culture growth. Sample reflectance spectra are displayed in **Error! eference source not found.**, accompanied by fits to the reflectance model described by Reichardt et al. (2012). In order to fit the spectra, the relative amplitudes of the absorption features of *Nannochloropsis* sp. (Gitelson, 2000) were no longer fixed within designated pigment groupings, as described by Reichardt et al., but ra ther were allowed to vary independently. In addition, the backscattering spectrum was approximated to be spectrally flat. **Error! Reference source not ound.** displays a comparison between the backscattering coefficient and the dry cell weight (DCW) determined from sampling measurements acquired daily. The linear scaling of the two vertical axes has been set to illustrate the agreement

between the algal backscattering coefficient and the DCW. As expected, the algal

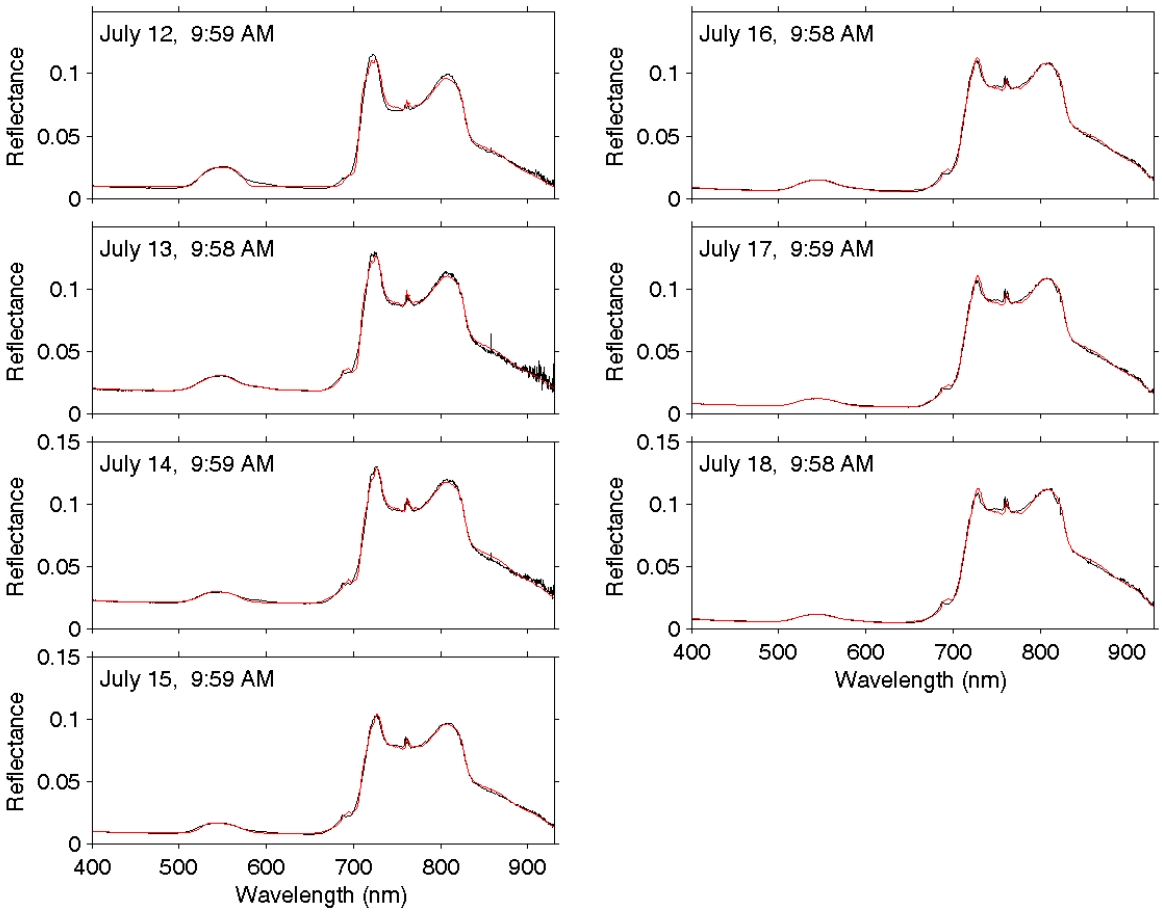

Figure 2-5 Reflectance spectra acquired at ~10 AM each morning for the first 7 days of culture growth. T he data are displayed with black lines, while the model fits are displayed in red

backscattering coefficient increases with increasing algal density, providing a remote assessment of biomass.

2.5. Conclusions and Future Outlook

Hyperspectral reflectance provides the capability to monitor remotely the algal pigment optical activity and algal cell backscatter. The hardware required for such a measurement is of reasonable cost (~$10K) and is sufficiently rugged for long-term autonomous field deployment. Challenges nevertheless remain in the quantitative interpretation of data, including

(a) the variable angle of the sunlight and the resulting specular reflection from the water surface (Doxaran, 2004b; Lee, 2010; Singh, 2008),
(b) potentially rapidly changing sunlight conditions due to shading (Adler-Golden, 2001; Doxaran, 2004a) or variable clouds (Adler-Golden, 2009),

(c) the uncertainty in defining the backscattering spectrum for any specific algal species (Ahn, 1992; Craig, 2006; Doxaran, 2009; Quirantes, 2006; Stramski, 2001; Svensen, 2007; Vaillancourt, 2004; Whitmire, 2010; Zhou, 2012),
(d) the spectral variation of the angular extent of the reflected light field (Hirata, 2009; Hlaing, 2012; Lee, 2011; Morel, 1996; Zibordi, 2001).

Addressing these challenges is an area of active research within the field of oceanography. Having demonstrated that implementation of the approaches of the oceanography community are appropriate for assessing algal biofuel production, it is anticipated that algal remote monitoring will continue to benefit from their ongoing advances.

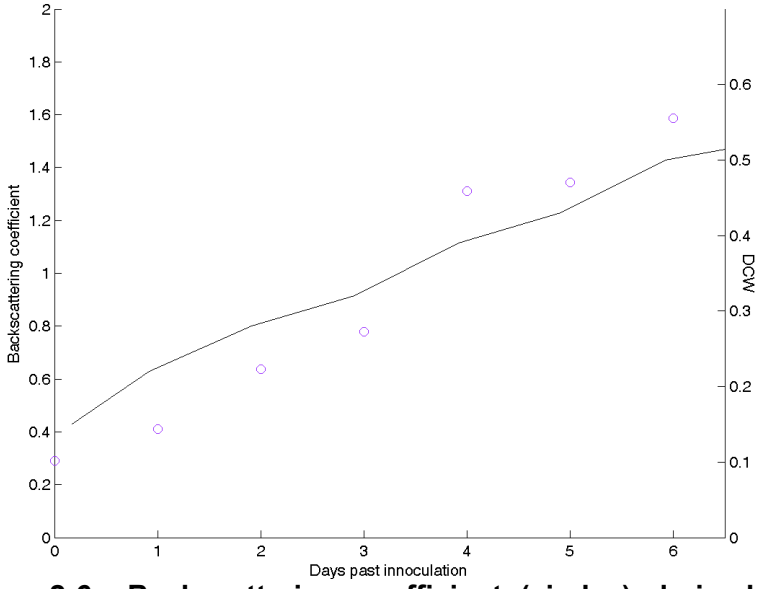

Figure 2-6 Backscattering coefficient (circles) derived by fitting the spectra displayed in Fig. 5 compared to the DCW (line) determined via sampling.

3. UNDERSTANDING THE ROLE OF THE CCM IN ALGAL GROWTH AND LIPID PRODUCTION UNDER NORMAL AND STRESS CONDITIONS

3.1. Introduction

Algae are an extremely diverse and artificial grouping of organisms that span the tree of life, differing more from each other than humans from some algae. In the broadest interpretations, the term "algae" even includes prokaryotes (cyanobacteria and some proteobacteria). Despite these differences, they share the same core photosynthetic carbon metabolism based on the Calvin cycle. Many appear to have evolved add-ons to the core processes, though few have been tested. One common add-on is a pyrenoid-based carbon concentrating mechanism (CCM) (Badger, 1998). The pyrenoid is an electron-dense proteinaceous body within the chloroplast and is repeatedly spanned by a network of thylakoid membranes. It is primarily composed of the CO_2 capturing enzyme ribulose-1,5-bisphosphate carboxylase oxygenase (Rubisco), carbonic anhydrase, and a few other enzymes involved in the Calvin cycle. The function of the pyrenoid is to localize Rubisco and carbonic anhydrase to a region within the chloroplast where CO_2 is elevated through the action of cellular CO_2 and HCO_3^- pumps. This effectively eliminates the oxygenase activity of Rubisco and increases the efficiency of photosynthetic CO_2 capture. The pyrenoid CCM is also variably expressed in many algae, being down regulated in environments where CO_2 and HCO_3^- levels are high and up-regulated when they are low. It is not known if the expression of the pyrenoid CCM has an impact on the production of lipids. In fact, even the presence or absence of a pyrenoid CCM in most potential algal biofuel production species is unknown.

Understanding the efficiency of CO_2 capture and conversion to lipids in algae is essential for engineering and operation of an algal biofuel facility. The provision of CO_2 is costly both energetically and economically, and the cost increases substantially if CO_2 levels within cultures need to be maintained above atmospheric. At atmospheric CO_2 levels, algae expressing a CCM can photosynthesize at the same rate as cells growing at 1-5% CO_2. However, this requires extra investment by the cell to energize the CCM and to synthesize extra proteins. These additional energy requirements could be met through additional light harvesting or consumption of lipid reserves. It is also reasonable to hypothesize that low CO_2 would be perceived as a stress, much like low nitrogen, and stimulate cells to store dramatically more lipid. Each of these outcomes has significant implications for life-cycle analyses of an algal biofuel production facility.

This work examines the effect of CO_2 supply on both CCM function and lipid production by growing *Nannochloropsis salina* strain 1776 in cultures bubbled with high or low concentrations of CO_2 and then switching cultures between conditions. It is unknown if *N. salina* 1776 has a CCM, though *Nannochloropsis gaditana* has been shown to express one (Huertas, 2002). In addition, experiments conducted with *Chlamydomonas reinhardtii* have shown that providing CO_2 at or above 5000 ppm down-regulates CCM expression whereas providing CO_2 at or below 500ppm up-regulates CCM expression (Vance, 2005). Therefore, by switching cultures between 5000 ppm (high CO_2) and 500 ppm (low CO_2) and monitoring a time-course of their adaptation to each condition, we should be able to determine if there is a relationship between CCM function and lipid production. It should be noted, that this treatment is changing the total amount

of inorganic carbon (CO_2 and HCO_3^-) available ten fold, though the absolute amounts of either CO_2 or HCO_3^- depends on the pH, salinity, and possibly the carbonic anhydrase content of the media.

3.2. Description of Integrated Experiments Conducted

3.2.1. Algal growth and sampling

N. salina strain 1776 was grown in custom-built 500mL polycarbonate airlift photosynthetic bioreactors (Figure 3-1) using F/2 media adjusted to pH 7.6. Media was continuously added via a peristaltic pump at a flow rate of approximately 300 mL day^{-1} for cultures grown at high CO_2 and 150mL day^{-1} for cultures grown at low CO_2 in order to maintain similar cell densities in mid-log phase growth during the experiment. Cultures were continuously bubbled at a flow rate of approximately 100 mL min^{-1} with either approximately 5500 ppm (high) or 500 ppm (low) CO_2 in air and provided all mixing for the cultures. Fluorescent lights were kept on continuously and provided approximately 145 µmol photons m^{-2} s^{-1}. Culture temperature was 25°C. pH was monitored daily as cultures were grown for seed stock and then at each time point during the experiment. Initially, two seed cultures were grown for 3-5 days in two photobioreactors, one at each CO_2 level. Three days prior to the experiment, 150 mL was taken from each seed reactor and split equally to start three identical photobioreactors for each condition.

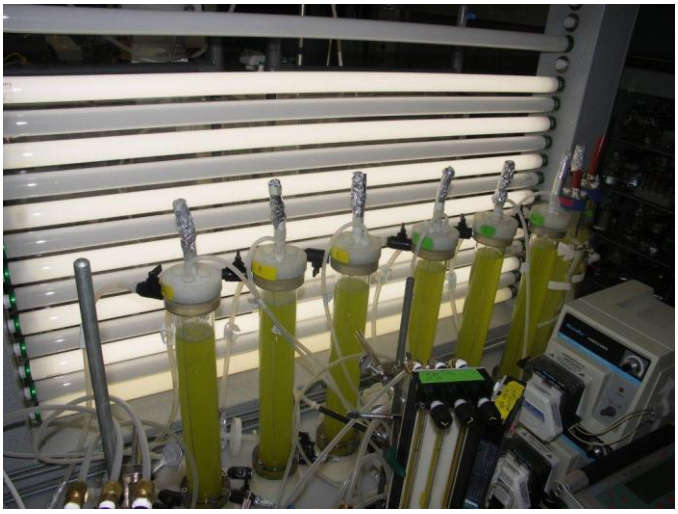

Figure 3-1 Airlifit photobioreactors. Filtered air was provided from the bottom and, along with a vertical baffle, was used to mix the cultures and to deliver CO2. Media was added continuously from the top using peristaltic pumps and overflow out the black valves at the top was collected for disposal.

Cultures started at low CO_2 were switched to high CO_2 in order to suppress CCM function and cultures at high CO_2 were switched to induce CCM function. Six cultures (3 for each treatment) were sampled at four time points: 0, 4, 24, and 48 hours after switching the concentration of CO_2 supplied to the culture to monitor the rate of adjustment to each condition. All sampling began about 60 minutes prior to each time point so that sample collection was complete by the designated time. At each time point ~25 mL of culture was removed through a valved port at the base of the photobioreactor and the pH was measured. Precisely 10 mL of the sample was pelleted, frozen, and stored at -80 °C for future analyses. Five 5 mL of sample was placed into a glass tube for measurements of variable chlorophyll fluorescence, 1 mL was pelleted and frozen in liquid nitrogen for chlorophyll extraction, 1 mL was used to determine the rate of photosynthesis via net oxygen exchange, and 5 mL were used for flow cytometry and microscopy (BODIPY staining, spinning disk fluorescence microscopy, and hyperspectral imaging). Air entering and exiting the culture was

also collected in Tedlar bags with gas ports for later determination of photosynthesis via net CO_2 exchange and photosynthetic discrimination.

3.2.2. BODIPY staining and flow cytometry

1.5 ml of culture from each PBR was mixed with 15 uL of bodipy (1mM stock) to a final concentration of 10 uM, and incubated for 5 minutes at room temperature. 100 µL aliquots were then removed for cell counting and analysis on a flow cytometer. Three dilutions ranging from 1:20 to 1:100 of each BODIPY labeled into culture media were analyzed using the Accuri flow – "slow fluidics" setting until 20,000 events above background were collected.

3.2.3. Chlorophyll extraction

Frozen 1 mL pellets were resuspended in cold methanol via vortexing. This freeze-thaw step was essential for complete extraction (data not shown). Cell debris was pelleted via centrifugation and the supernatant was assay spectrophotometrically for chlorophyll a content (Porra, 1989).

3.2.4. Variable chlorophyll fluorescence

Pulse-amplitude modulated variable chlorophyll fluorescence (Mini-PAM, WALZ, Inc) was measured at each time point to assess the efficiency of linear electron transport originating from PSII(Genty, 1989). Samples were measured in the light (Fv'/Fm') and after 20 min of dark adaptation (Fv/Fm).

3.2.5. Net oxygen exchange

An oxygen electrode (Hansatech, Inc) was maintained at culture temperature (25^{o}C), illuminated with a fluorescent bulb (145 µmol photons m^{-2} s^{-1}), and calibrated daily with water sparged with air (20.9% O_2) or nitrogen. Rates of net photosynthetic oxygen production were determined from the slope of the increasing O_2 concentration immediately after transferring a 1mL aliquot from the photobioreactor to the electrode cuvette. Rates were expressed on a per cell and per mg chlorophyll a basis.

3.2.6. Net CO_2 exchange and photosynthetic discrimination

Gasses entering and exiting each photobioreactor were collected in Tedlar bags at each time point. Gas bags were then transported to the University of New Mexico (UNM) and analyzed for total $^{12}CO_2$ and $^{13}CO_2$ content using a tunable diode laser (TDL) absorbance spectrometer (TGA-100, Campbell Sci.). Each bag was connected to a TDL inlet and sampled at a rate of 100 mL min^{-1} until a steady signal was achieved (usually1-2 min). The TDL uses a Nafion counter-flow system to dry all samples to a constant water content and two standards were sampled every 10 min for calibration. All calibrations for each day were used to determine and offset and gain that were each fit by a spline function. This spline was used to generate offsets and gains during the time for each bag sampling in order to correct for slow instrument drift between calibrations. Net photosynthetic CO_2 assimilation was then determined from the difference in total CO_2 concentration between air entering and exiting the photobioreactor after correcting for flow rate. Rates were determine on both a per cell and a per chlorophyll a basis. Photosynthetic discrimination (Δ, the preferential capture of $^{12}CO_2$ over $^{13}CO_2$) was determined from the change in the isotopic composition ($\delta^{13}C$) of air entering and exiting the photobioreactor relative to the rate of net photosynthetic CO_2 assimilation (Barbour, 2007; Sharkey, 1985).

3.2.7. Hyperspectral confocal and spinning disk fluorescence microscopy

Hyperspectral confocal fluorescence images were collected for both BODIPY stained and unstained (BG-38 filter) samples and analyzed using multivariate curve resolution (MCR). Hyperspectral confocal fluorescence microscopy and multivariate curve resolution analysis are described in more detail in Section 5 and in the literature (Jones, 2012; Sinclair, 2006). MCR identified four components in the unstained cells that represent the major algal pigments shown in Figure 3.2: a lipid-body associated carotenoid, chlorophyll *a*, a chloroplast associated carotenoid, and a carotenoid not associate with the chloroplast or lipid bodies. These were used for subsequent analyses. In addition to their independent analyses, the lipid associated carotenoid component was also quantified as a ratio relative to the chlorophyll a component on a per cell basis.

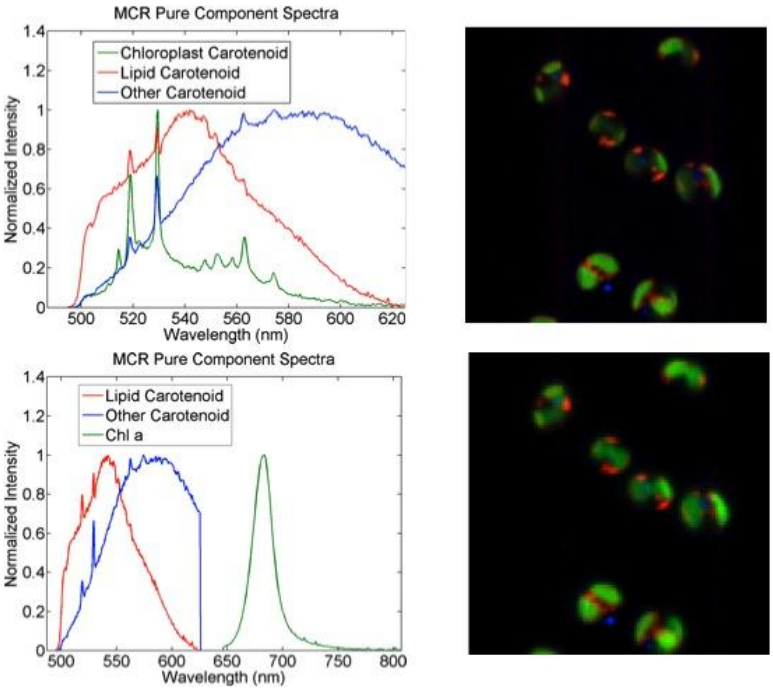

Figure 3-2 Multivariate curve resolution from hyperspectral imaging. This analysis identified four major components of the non-stained cultures that could separate out lipid droplets and chloroplast, along with some other unknown signals.

3.3. Results and Discussion

3.3.1. Growth and photosynthetic response

Growth rates of *N. salina* 1776 were consistent at each CO_2 level during the 48-hr experiment as shown by the maintenance of a relatively constant cell density under a constant rate of media exchange (Figure 3-3A). The differences in cell density between conditions at time 0 hr were primarily due to different densities of the seed cultures grown at each CO_2. Small errors in the estimation of the media flow rate needed to keep both sets of cultures at the same density may have also contributed, however, the consistency of the cell density between time 0 and 48 hr shows that the flow rates used were suitable for the experiment. Maintaining similar cell densities between conditions was desired since cell density can have an independent effect on rates of cellular respiration (DeLong, 2009a; DeLong, 2009b). The slight decline in mean density by the end of the experiment in cultures that were started at high CO_2 and switched to low CO_2 at time 0 hr correlates with a decline in net photosynthetic O_2 exchange (Figure 3-3B) and an increase in pH (Figure 3-4).

Measures of photosynthetic function showed different responses to the changing CO_2 conditions. Net photosynthetic O_2 production (Figure 3-3B) initially increased in both treatments. Cultures

that moved into high CO_2 (low start) then dropped back to the rates at 0 hr and leveled out. However, cultures moving from high to low CO_2 (high start) continued to decline after the initial increase at 4 hr. Similar patterns were seen when examining photosystem II (PSII) yield in the light, though declines for the high start cultures were not seen until between 24 and 48 hr (Figure 3-3C). The quantum efficiency measured as Fv/Fm in dark adapted samples decreased consistently with time after 4 hr (Figure 3-3D). Low quantum efficiencies are often associated with stress and could indicate PSII damage. Net photosynthetic CO_2 uptake increases between 0 and 4 hr in cultures switched from low to high CO_2 (similar to net O_2 release), but then levels out at the higher rates (Figure 3-3C). In contrast, net photosynthetic CO_2 uptake decreases between 0 and 4 hr in cultures switched from high to low CO_2 (opposite of net O_2 release), and then levels out at the lower rates rather than declining like net O_2 release. In addition, net O_2 release is consistently several fold higher than net CO_2 uptake which suggests that there is much greater electron transport than is needed for CO_2 assimilation.

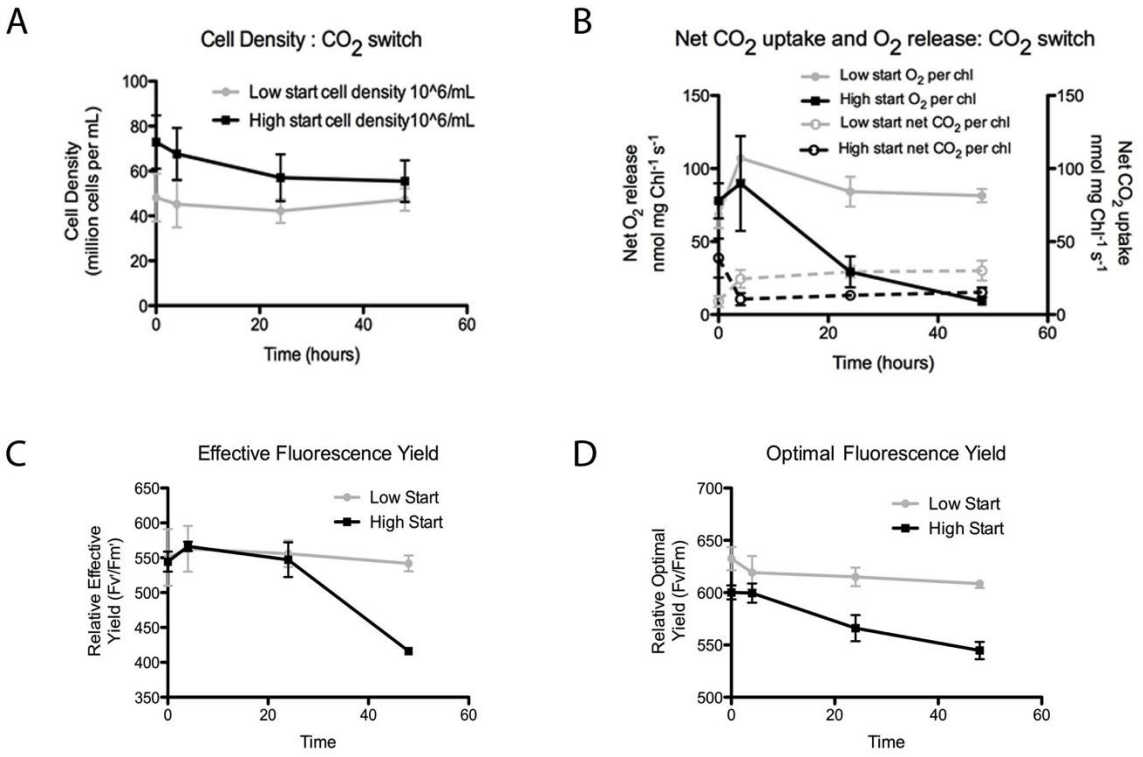

Figure 3-3 Growth and photosynthetic response. A. Cell density during the experiment. Flow rates of liquid media were switched simultaneously with changing the concentration of CO2 supplied such that cultures receiving high CO2 always had about twice the flow rate as cultures receiving low CO2. B. Net photosynthetic CO_2 uptake and O_2 release. Rates of CO_2 exchange were determined from the fluxes of air entering and exiting the photobioreactors. Oxygen exchange rates were determined by measuring culture aliquots with an oxygen electrode set at the same light intensity and temperature as the photobioreactors. C. Relative electron transport yield measured via variable chlorophyll fluorescence in the light. D. Relative quantum efficiency of electron transport measured via variable chlorophyll fluorescence in dark-adapted samples.

3.3.2. Discovery of regulated CCM function in N. salina strain 1776

The excess O_2 release relative to CO_2 uptake is consistent with the observations of an unusual CCM that has been characterized in *N. gaditana* (Huertas et al., 2002). The *N. gaditana* response has been characterized as a "pump-leak" CCM that pumps large amounts of HCO_3^- into the cell from the surrounding media, but then also leaks much of it back out in the form of CO_2. In fact, the activity of this CCM can be so great that there is an apparent net CO_2 loss at the culture level. Essentially, the HCO_3^- is pumped in and converted to CO_2 much faster than Rubisco can capture it. This pumping requires ATP, which in the case of *N. gaditana* is at least partially supplied through mitochondrial respiration. These observations in *N. salina* are consistent with those of *N. gaditana*, though mitochondrial respiration may not be needed for the ATP. Further experiments are needed to determine the involvement of mitochondria.

Unlike all but one prior study in algae (Sharkey and Berry, 1985), we have developed a method for measuring preferential use of $^{12}CO_2$ over $^{13}CO_2$ during photosynthesis as a method for detecting CCM function. Our method is novel, in that it makes these measurements in real-time (10 Hz), avoiding the need to capture, dehydrate, and then isotopically analyze CO_2 isotopic composition at static points, and this is demonstrated in the proof of concept work. The data presented here are a slight modification where samples were collected in bags prior to analysis since the isotope analyzer was too large to bring to SNL where the hyperspectral data had to be collected. The only effect of this was to limit the collection to discrete time points. As shown in Figure 3-4, there is a large change in photosynthetic discrimination within 4 hr of switching CO_2, increasing discrimination when switching to low CO_2 and decreasing when switching to high

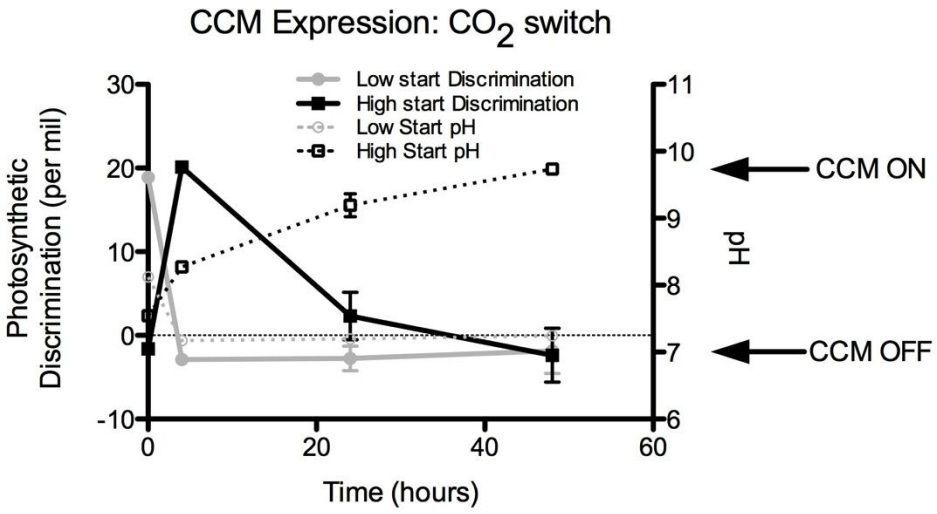

Figure 3-4 Photosynthetic discrimination and pH. High photosynthetic discrimination was used to indicate that CCM activity was present while low discrimination indicated the absence of CCM activity. This is opposite of the expected CCM signal due to the unusual pump-leak style CCM found in *Nannochloropsis*. pH is also shown here to highlight that the decrease in discrimination after 4 hours of exposure to low CO_2 was correlated with an increasing pH in cultures that were stable at high CO_2 prior to switching.

CO_2. However, 4 hr after the rapid switch to low CO_2, discrimination decreases in parallel with the decline of net O_2 release.

Large changes in discrimination in response to the inorganic carbon content around cells is a strong indicator CCM function and is the best evidence of a CCM functioning in *N. salina*. This is because large changes in discrimination are caused by changes in how leaky cells are to CO_2 with higher discrimination for leakier cells (Sharkey and Berry, 1985). Normally, a CCM reduces leakiness of a cell and decreases discrimination. However, the unusual "pump-leak" CCM of *N. gaditana* would be likely to have the opposite signature since is becomes more leaky

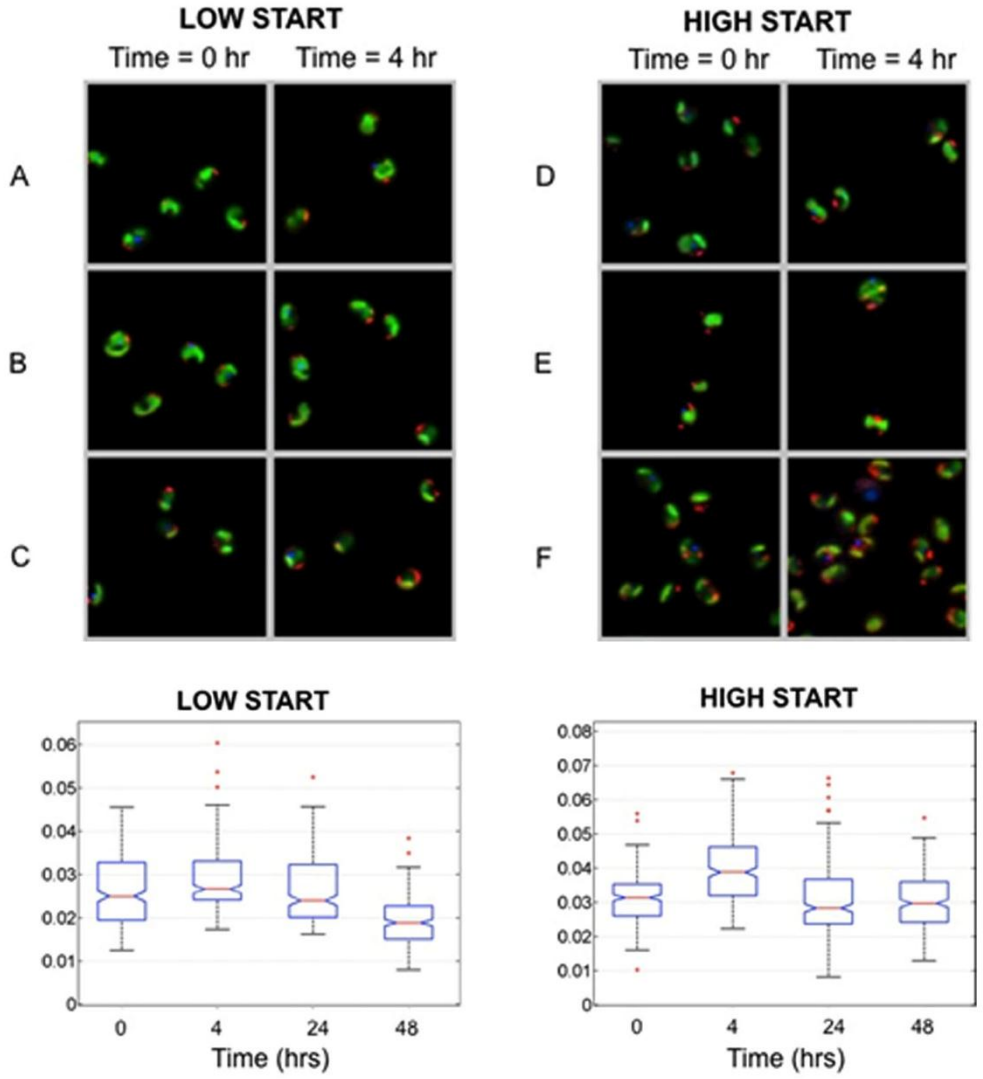

Figure 3-5 Top Panels: Representative hyperspectral images after MCR analysis from each culture at time 0 and 4 hr. Cultures A-C started at low CO2 and D-F started at high CO2. Representative images were selected from those that were near the mean ratio of lipid to chlorophyll Bottom Panels: Box and whisker plot showing the relative lipid to chlorophyll content per cell. Notches represent the 95% confidence limits, so times where notches to not overlap are significantly different.

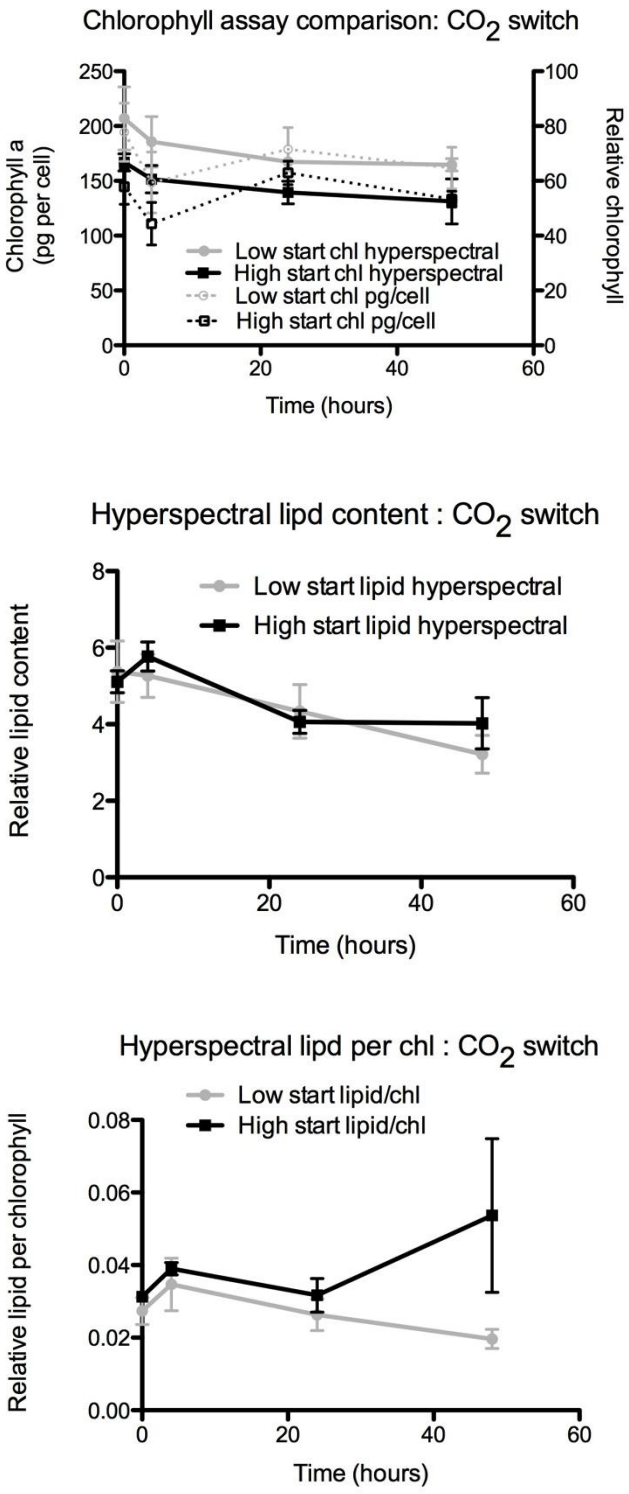

Figure 3-6 Chlorophyll and lipid content as determined by hyperspectral imaging and analysis. Top: Comparison of the bulk chlorophyll assay with hyperspectral imaging. Middle: Relative lipid content. Bottom: Ratio of lipid content to chlorophyll content per cell.

with respect to C O_2 when the CCM is functioning. Since *N. salina* becomes leakier at low CO_2, we believe that it has a "pump-leak" CCM like that of N. *gaditana*. Interestingly, the induction of CCM function upon transfer to low CO_2 is transient, though it's suppression at high CO_2 was not. We hypothesize that this may be due to the sudden onset of stressful low CO_2 conditions where a leaky CO_2 system has the leaked CO_2 stripped away into the atmosphere due to the bubbling rather than building up in the surrounding media. This stress could explain the drop in O_2 release, decline in PSII function, and the increase in pH. However, we should note that *N. salina* can grow in the low CO_2 conditions as they were growing well in the seed cultures. It is possible that the initial seed cultures were started in a manner that more gradually exposed the cells to low CO_2.

3.3.3. Lipid production response

Lipid content per cell normalized to chlorophyll content was determined using hyperspectral imaging and multivariate curve resolution (MCR) techniques developed at SNL (Figures 3-5 and 3-6). This analysis was done only without exogenous staining and section 5 describes comparisons of this method with that of BODIPY staining. The MCR identified independent spectral components representing lipid body associated carotenoid and chlorophyll *a*, along with a chloroplast associated carotenoid signal overlapping spatially with chlorophyll a, and a non-plastid, non-lipid carotenoid (Figure 3-2). Representative imaging of cells are shown in Figure 3-5 top panel. Changes in the chlorophyll *a* signal per cell were consistent with changes in the bulk culture chlorophyll *a* content determined from methanol extractions (Figure 3-6 top panel).

The lipid signature showed a small increase in the amount of lipid between 0 and 4 hr before declining in the cultures that were switched from high to low CO_2 whereas the lipid content in the low to high switched cultures consistently dropped with time (Figure 3-6 middle panel). However, when lipid content is expressed per chlorophyll *a*, the pattern changes slightly. In this case, both treatments show an increase between 0 and 4 hr (Figure 3-6 bottom panel) though the increase only reaches significance at the 5% level in the high to low CO_2 transition treatment (Figure 3-5, bottom panel). In both cases, lipid content returns to starting levels after 4 hr. It should be noted that the lipid changes were modest making them difficult to detect without the analytical and statistical power provided by the MCR analyses.

3.5. Conclusions and Future Research

Interactions between CO_2 supply, CCM function, and lipid production were evident in this experiment. It is clear that low CO_2 induces a CCM in *N. salina* and that the CCM is suppressed at high CO_2. This is the first demonstration of CCM function in *N. salina* and is supported by comparisons of net O_2 and CO_2 exchange along with changes in the usage of CO_2 isotopologues. The interaction with lipid production is less clear and may be improved upon completion of bulk measures of lipid content. However, it does appear that a transient increase in lipid production occurs when CO_2 supply is altered, and that per cell the lipid content is very similar whether cells are grown with high or low CO_2. This suggests that investment in supplying high levels of CO_2 may not be warranted as the CCM of *N. salina* maintains sufficient carbon for lipid production even when only ambient air is provided. Simply a 4 hour boost in CO_2 may be all that is needed to increases lipid synthesis. However, this experiment did not allow for changes in cell density through the continuous addition of culture media and the air bubbling also kept inorganic carbon levels from building up in the media after leaking out of the cells. The extra nutrients provided, the consistent density of cells, and the bubbling could all have independent effects on the production of lipids. Additional experiments under different conditions should determine if differences in engineering or biological function will maintain the same relationships between CO_2 supply, CCM function, and lipid production in other culture systems.

4. DEFINING THE BOUNDARY BETWEEN STRESS AND PROGRAMMED CELL DEATH IN A MODEL ALGA

4.1. Introduction

"Pond crashes," where target algal strain(s) rapidly die, represent fundamental bottlenecks in scalable algal biofuels production. These events result from both biotic and abiotic stressors, such as pathogens/pest exposure, temperature fluctuation, high salinity as a consequence of evaporation, and nutrient depletion. Abiotic drivers of these sudden, poorly understood die-offs (*e.g.*, oxidative stress, elevated temperatures and high salinity) are believed to promote programmed cell death-like (PCD) responses in members of the green algae (taxonomic divisions Chlorophyta and Charophyta in kingdom Plantae), but information clearly linking genetic, physiologic and even organismal-level responses to factors possibly associated with these processes is limited and frequently ambiguous. To address basic information gaps in "pond crashes," we investigated PCD-like processes in *Chlamydomonas reinhardtii* and attempted an initial mapping of the boundary between physiologic stress and cell death. *C. reinhardtii* is the focus of this work because it is the premier green algal model for biochemistry, classical genetics and genomics, and these resources enabled multi-scale, multi-dimensional lines of inquiry (Merchant, 2007). Approaches developed here, including genome-wide monitoring of expression patterns, tracking of spectral signatures associated with biological pigments, and surveying gross cellular morphological changes, represent potentially fieldable technologies for pond health and productivity.

4.2. Description of Integrated Experiments Conducted

In the work summarized here, the genetic, physiological and morphological effects of different salinity levels (150 mM, 250 mM and 1M NaCl) were investigated in the model green algal species *C. reinhardtii* to give a detailed account of early, middle and late molecular events associated with programmed cell death (PCD) *versus* basal stress responses. Recent reports have shown that elevated salinity induces PCD in both higher plants and green algae, but these studies fail to provide fine-grained insight into this phenomenon (Affenzeller, 2009; Clarke, 2000; Greenberg, 1996; Moharikar, 2006). PCD studies in fresh water green algal species, such as *Micrasterias denticulata*, typically have presented results with morphological/ultrastructural and biochemical emphases, or have focused narrowly on expression of a few genes deemed important in genetically programmed death responses. To address fundamental information gaps about PCD versus physiologic stress in *Chlamydomonas*, experiments were designed to measure responses to different levels of salinity mentioned above. Experimental conditions examined here were suggested by published literature as well as pilot studies conducted in the early phases of this project that explored both the type and level of PCD-inducing factors considered for broader inquiry. Key findings include altered pigment composition, changes in gross morphology, severely diminished cell viability and differential gene expression.

4.2.1. Algal growth and physiological measurements

4.2.1.1 Strain

C. reinhardtii CC-125 wild type mt+ (aka 137c) (for more info, see: http://chlamycollection.org/strain/cc-125-wild-type-mt-137c/). The sequenced strain, CC-503 cw92 mt+, a cell-wall deficient mutant, is derived from CC-125 (Merchant, 2007).

.

4.2.1.2 Culturing conditions

C. reinhardtii CC-125 was maintained on tris-acetate-phosphate (TAP) agar medium (Gorman, 1965). Single colonies were removed aseptically to liquid TAP medium and shaken continuously at 150 rpm and 23°C in an Innova 42 shaker series incubator (New Brunswick Scientific; Enfield, CT). Cultures were grown under continuous light. When optical density at 750 nm (Lamda Bio, Perkin Elmer; Waltham, MA) reached approximately 0.6 cultures were used for experimentation. No antibiotics were added to liquid TAP medium; contamination of cultures by bacteria was monitored by plating liquid medium onto LB agar (20g LB Broth [Fisher Scientific; Waltham, MA], 20 g Difco agar [BD Biosciences; San Jose, CA], 1 L water) plates and by inspecting small culture volumes with light microscopy. Contaminated cultures were discarded.

4.2.1.3 Assessment of photosynthetic efficiency

Pulse amplitude modulated (PAM) fluorescence was measured using a Waltz Mini-PAM chlorophyll fluorometer. The quantum yield of photochemical conversion (F_v'/F_m') was determined for each culture by taking 3 technical replicate measurements and reporting the average.

4.2.1.4 Measurement of Reactive Oxygen Species (ROS)

Reactive oxygen species (ROS) were detected using 2,7-dichloro fluorescein diacetate (H_2DCFDA, Invitrogen). H_2DCFDA was added to 500 µL of control and experimental cultures to a final concentration of 1.02 µM from a stock of 1.02 mM H_2DCFDA dissolved in dimethyl sulfoxide (DMSO). DMSO was also added to a final concentration of 2% to increase cell membrane permeability. The mixture of cells, H_2DCFDA and DMSO was placed in a plastic microcentrifuge tube, and incubated under standard growth conditions for 1 hour. After this period, the mixtures were analyzed using an Accuri C6 flow cytometer. For each sample, 20,000 cells were analyzed for fluorescence emission at 533 nm (30 nm bandwidth), and cells with increased fluorescence emission were considered to be positive for ROS.

4.2.1.5 Rates of cell death in response to high salinity

Cell viability in control and experimental treatments were assayed throughout the experiment using the mortal nucleic acid stain SYTOX Green (Life Technologies, Grand Island, NY). Sample aliquots (300 µL of control and experimental cultures) were incubated with 300 nM Sytox for 30 minutes in darkness at room temperature. Mixtures were analyzed on the Accuri C6 flow cytometer described above (4.2.1.4). Cells with compromised cells membranes, which are not viable, had green emission ~100 fold higher than control cells, and this metric was used to determine the ratio of live:dead in samples

4.2.1.6 Oxygen evolution to monitor rate of photosynthesis.

The rate of oxygen evolution was measured for each culture using a calibrated S1 Clark type electrode and measuring system from Hansatech Instruments (Norfolk, England). For each reading, 1 mL of sample was added to the instrument chamber for analysis. The sample was illuminated with a fluorescent light source at an intensity of 125 µmol photons m^{-2} s^{-1}, and the culture was mixed with a magnetic stir bar at 100 rpm.

4.2.2 Molecular biology

4.2.2.1 RNA isolation and complementary DNA synthesis

At each timepoint (0, 1, 3, and 5 h) two 75 ml samples were collected from each experimental condition. Cells were pelleted by two centrifugation steps (1000 x g for 3 minutes at 4 C [Allegra X-30R Centrifuge, Beckman Coulter; Indianapolis, IN] in sterile 50 ml tubes. Culture supernatant was decanted, cell pellets were re-suspended in small volumes [1-2 ml] and transferred to 2 ml microcentrifuge tubes. Samples were centrifuged again at 1100 x g for 1.5 min [Centrifuge 5424, Eppendorf; Hauppauge, NY] and the supernatant was removed with a pipet.) Cell pellets were flash frozen with liquid nitrogen and stored at -80 C until RNA isolation.

RNA was isolated with an RNeasy Plant Mini-Kit (Qiagen; Valencia, CA). Cell pellets were re-suspended in RLT lysis buffer and vortexed vigorously; after this step, the manufacturer's protocol was followed. RNA samples were also treated with DNase twice (according to RNeasy protocol: the first treatment was done during RNA isolation and the second before performing optional RNA clean-up steps). RNA quality was accessed with a RNA 6000 Nano chip (Agilent Technologies; Santa Clara, CA), run on a 2100 Bioanalyzer with 2100 Expert software (Agilent Technologies, Santa Clara, CA). RNA quality and quantity were evaluated by measuring the absorbance at 260, 280, and 230 nm with a Nanodrop 2000 (ThermoScientific, Rockford, IL). RNA elutions with degraded RNA or low quality/quantity scores were not used in later steps. RNA was stored at -80°C until construction of complement DNA (cDNA).

cDNA was synthesized with the QuantiTect Reverse Transcription Kit (Qiagen; Valencia, CA). A total of 1 µg of RNA was added to each library preparation and the manufacturer's protocol was followed. Since expected cDNA fragment sizes were approximately 200bp, the synthesis step was extended from 15 min to 30 min as suggested by the Qiagen protocol. cDNA was stored for less than 24 h at -20°C before use in quantitative real-time polymerase chain reaction assays.

4.2.2.2 Quantitative real-time polymerase chain reaction.

Quantitative real-time polymerase chain reaction (qRT-PCR) assays were set-up on ABI Prism 96 well Optical Reaction Plates (Applied Biosystems; Foster City, CA) with the following recipe for each reaction: 50 µl Sybr Green (Applied Biosystems; Foster City, CA), 47 µl sterile DEPC treated water (MoBio Laboratories, Inc.; West Carlsbad, CA), 1 µl 10 mM forward primer, 1 µl 10 mM reverse primer, 1 µl of cDNA preparation. Each plate also included control reactions that contained RNA elutions (diluted to match total nucleic acid concentrations in cDNA preparations) instead of cDNA to verify that gDNA was not responsible for any detected amplification. Plates were sealed with MicroAmp Optical Adhesive Films (Applied Biosystems; Foster City, CA) and qRT-PCR assays were run on a 7500 Real Time PCR System with 7500 Software v. 2.0.5 (Applied Biosystems; Foster City, CA) with a 50ºC step for 2 min, and 95ºC for 10 min hot start, followed by the cycling and melt curve stages. The cycling stage program was as follows: 95ºC for 15s, 60ºC for 1 min, repeat for 40 cycles. The melt curve program was as folllows: 95ºC for 15 s, 60C for 1 min, 1% increase in temp every 30s until reaching 100ºC, 95ºC for 30s, and 60ºC for 15 s.

The Ct values for replicate wells were average and used to compute a 2^-ΔΔCt value for each treatment. When a Ct value was not established during qPCR (i.e., no detectable amplification) that sample was assigned a Ct value of 40.

4.2.3. Microscopy

4.2.3.1 Light microscopy

From each experimental condition, 1 ml of culture was removed at timepoints 0 h, 5 h, 10 h, 24 h, 48 h, and 72 h. The sample was centrifuged (1100 x g for 1 min [Centrifuge 5424, Eppendorf; Hauppauge, NY]) and the supernatant removed. Ten µl of the wet cell pellet was mixed with 4 µl of warm 1% low-melting point agarose and immediately loaded onto a microscope slide and covered with a micro coverglass. Widefield images were acquired on an Olympus IX71 microscope using a 60X oil immersion (NA=1.4) objective. A minimum of 30 cells were recorded for each time point.

4.2.3.3 Hyperspectral confocal fluorescence microscopy & analysis

Hyperspectral imaging was used to investigate temporal changes in the pigment distributions at the cellular and subcellular level as a function of salt stress. *C. reinhardtii* was subjected to three different salt concentrations over a period of nine hours. The three salt concentrations were as follows: 1) Control cells – No salt was added, 2) PCD cells – 0.25M NaCl was added to mildly stress the cells and induce PCD, and 3) Necrotic cells – 1M NaCl was added. Hyperspectral imaging occurred at the 3, 6 and 9 hour time points for the control and PCD salt concentrations, while the necrotic cells were only imaged at t=3 hrs. The hyperspectral imaging and analysis methodologies are described in more detail in Section 5 of this report. For this experiment, 300 nM Sytox Orange (Life Technologies, Grand Island, NY) was added to the cells before they were prepared onto microscope slides for imaging. The Sytox Orange was added to identify cells with compromised cell membranes.

4.3. Results and Discussion

4.3.1. Impact of salt stress on growth, morphology, and ROS

Bright-field microscopy analyses distinguished *C. reinhardtii* cells under physiologic stress, programmed cell death (PCD) and necrotic conditions over the extended time sampling points. Stressed cells (0.15M NaCl) showed evidence of cell membrane collapse away from the cell wall at the 24 hr time point, and had shifted to a palmelloid state at the 48 hr mark. Under PCD conditions, cell membranes pulled away from cell walls at the earlier 9 hr sampling point, and had also showed an earlier shift to the palmelloid state at 24 hr (Iwasa, 1969; Stern, 2008). Consistent with extra-nuclear morophological changes reported for in other organisms, cytosplamic blebbing at the 9hr and 24 hr time points is suggested prior to the shift to a palmelloid states in the PCD treatment (Figure 4-1). The single cells observed at the 48 hr time point show marked membrane shrinkage from the cell wall, and ovoid, bleb-like cytoplasmic features are evident. High salinity (1 M NaCl) resulted in whole-cell shrinkage (likely due to hyperosmotic milieu), and apparent evacuation of cell contents at the 48 hr time point. As expected, cells receiving the high salinity treatment did not transition through a palmeloid state.

The different salinity treatments (150 mM, 250 mM, 1 M NaCl) showed distinct cell viability and culture density (as measured by optical density) and effects (Figure 4-2). Cells under physiologic stress conditions (150 mM NaCl) do not divide at the same rate as untreated (control cells), but do not appear to be dying (as assessed by Sytox staining), whereas cells receiving the PCD – level of salinity (250 mM) showed high mortality (~ 70 % at 12 hr) and low culture

density. Most (> 90%) of these cells were dead at 24 hr. The majority cells (~ 80 %) in the necrosis-inducing treatment (1 M NaCl) took up Sytox orange at early sampling points (3 and 5 hr), indicating that death had occurred.

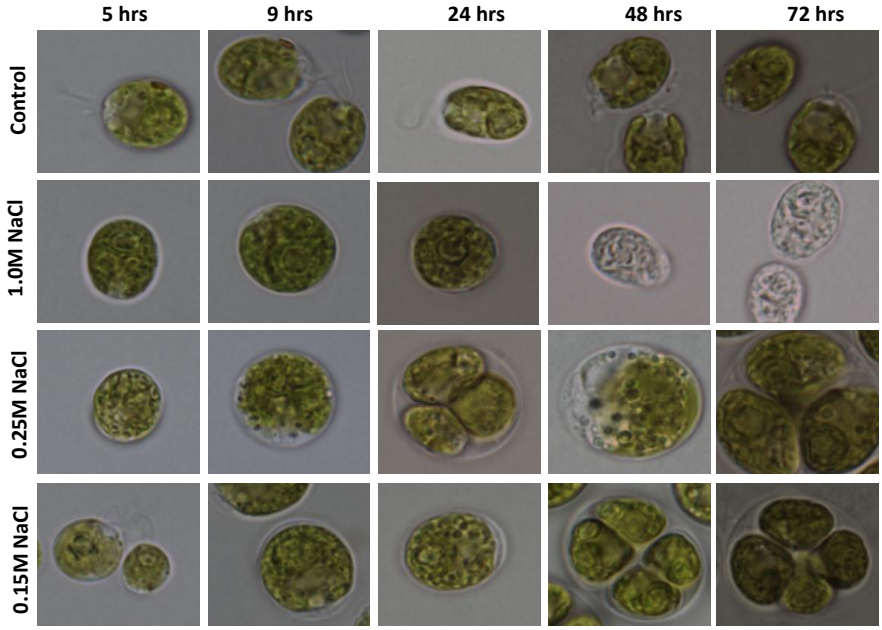

Figure 4-1 *C. reinhardtii* undergoes morphological changes under physiologic and stres and programmed cell death conditions

The generation of reactive oxygen species (ROS) ha s been linked to a variety of stress conditions, including both biotic and abiotic stressors (Apel, 2004). As their name suggests, ROS are highly reactive and cause intracellular damage by reacting with essential proteins. ROS have also been shown to serve as signals for activating gene expression, including PCD response in plants (Gechev, 2006). While elevated ROS levels have been found under both stress and PCD conditions in algae (Affenzeller, 2009), the role of ROS in each process has yet to be investigated. In this work, we analyzed the levels of ROS under all four conditions (0M, 0.15M, 0.25M, a nd 1M NaCl). In agreement with the literature, elevated ROS levels were detected in both the stress (0.15M NaCl) and PCD (0.25M NaCl) conditions. However, the rates of ROS generation varied between the stress and PCD conditions. Under the

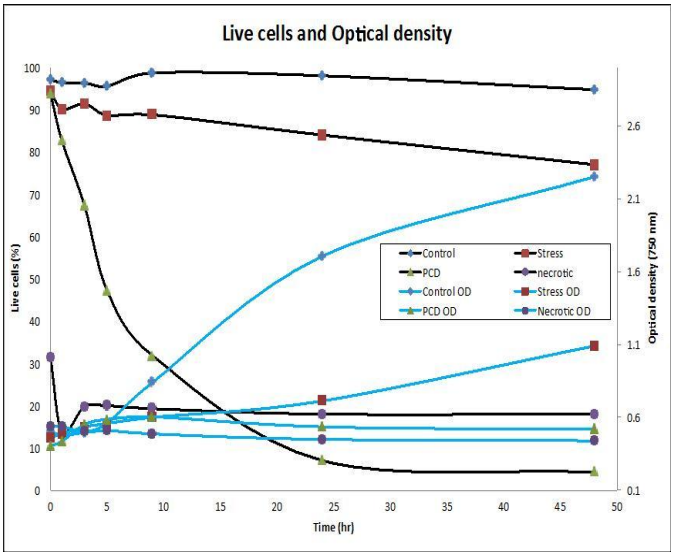

Figure 4-2 Different salinity treatment show distinct cell viability (black lines) and culture density (blue lines) effects.

PCD condition, ROS levels rapidly increased within the cell population of the *C. reinhardtii* culture. After 5 hours, approximately 40% of the cell population stained positive for ROS, compared to only 2% and 7% for the control and stress conditions at this time point. Under the stress condition, the rate of ROS generation was much slower, reaching similar ROS levels (i.e. 40% of the cell population) in 48 hours. These results confirm the involvement of ROS in both stress and PCD responses in *C. reinhardtii*, yet the rate of ROS production appears to be unique under each condition. PCD responses are characterized by a rapid rise in ROS levels within the first few hours of treatment, while a stress response elicits a gradual increase in ROS over the course of several days. This temporal variation in ROS generation may be essential in delineating between stress and PCD responses.

4.3.2. Impact of salt stress on pigment relative abundance and localization

Panels in Figure 4.3 overview the hyperspectral confocal microscopy experiments to assess temporal changes in the pigments of *C. reinhardtii* under salt stress. The MCR analysis revealed four spectral components (Sytox Orange, chlorophyll *a*, chlorophyll associated with the Light Harvesting Complex II and a chlorophyll shift component) shown in the upper left panel of Figure 4.3. Representative images of the control, PCD and necrotic cells are show in the bottom panel of Figure 4.3 and are colored accordingly to the component spectra. Red pixels increased with increasing concentration of NaCl, indicating a chlorophyll shift. This information is captured quantitatively in the boxplot (Figure 4.3, upper right). The red bar is the median value of the chlorophyll shift component in 20 cells and notches in the blue box represent a 95% confidence level. The presences of the chlorophyll shift becomes significant at t=6 hrs for the PCD cells. Notice that this shift also trends with the amount of time that the cells are subjected

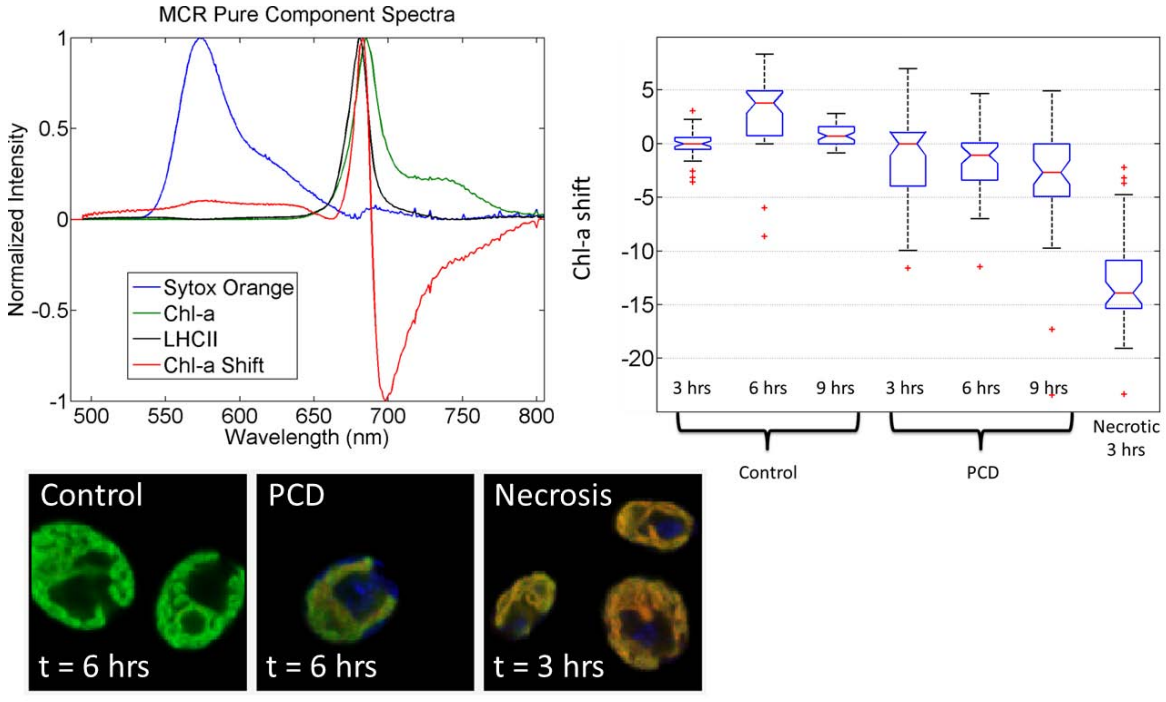

Figure 4.3: Hyperspectral confocal fluorescence microscopy results. Top left: MCR spectral components. Lower Left: RGB images using the color scheme associated with the spectral components (Blue = Sytox Orange, Green = Chl-a, Red = Chl-a Shift). Upper Right: Statistical box plot of the mean cell concentrations for the Chl-a Shift component.

to salt stress. The necrotic cells have the greatest chlorophyll shift relative to the control cells. Sytox Orange which penetrates compromised cell membranes had a similar trend to the chlorophyll shift (blue pixels increasing in the lower panel of Figure 4.3 and similar boxplot); indicating that this chlorophyll shift is associated with compromised cells (results not shown).

4.3.3. Impact of salt stress on photosynthesis

Impact of the different salinity treatments upon photosynthetic efficiency was assessed by measuring pulse amplitude modulated (PAM) fluorescence as well as oxygen evolution. The PAM fluorescence results (Figure 4.4) show that PCD and necrosis-inducing levels of salinity (250 mM and 1 M, respectively) significantly impair photosynthesis, consistent with the hypothesis that key organelles (*e.g.* cholorplasts) are structurally and functionally compromised in the PCD scenario, and that all cellular processes cease in necrosis treatments. Treatments inducing physiologic stress affect photosynthesis measurably, but effects observed in this scenario are much less dramatic than those observed in the other treatments. To validate trends observed in PAM measurements, evolved molecular oxygen, an indirect indicator of photosynthetic output, was also quantified. The evolved molecular oxygen results mirrors the PAM measurement results (not shown).

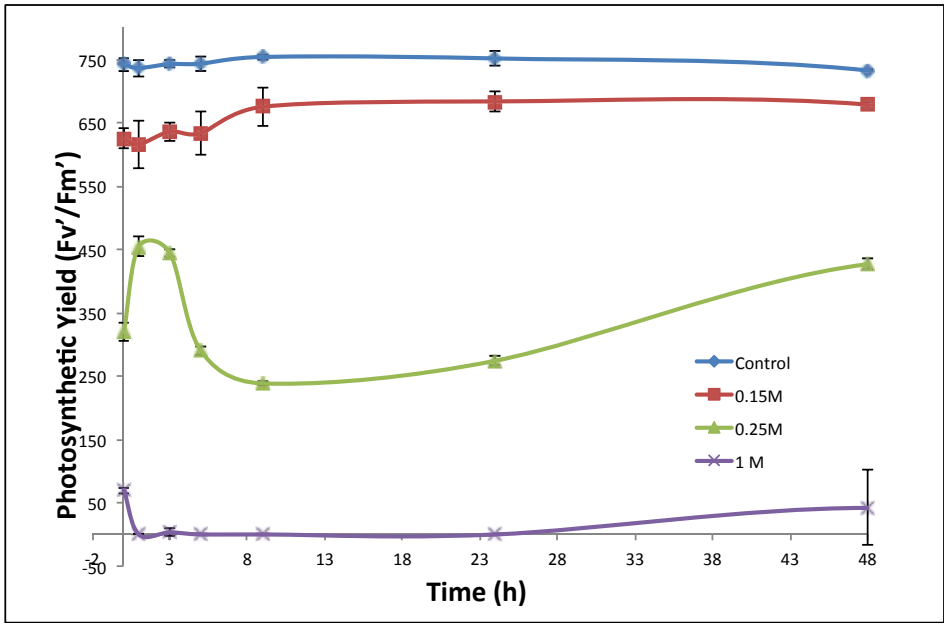

Figure 4.4 Changing photosynthetic efficiency under different salinity treatments. P hotosynthetic efficiency was diminished under all experimental conditions, with the necrosis-inducing treatment being the most affected, followed by those of the programmed-cell death (250 mM NaCl) and physiologic stress (150 mM NaCl).

4.3.4. Impact of salt stress on gene expression

To identify loci potentially involved in programmed cell death-like processes in *C. reinhardtii,* the *Arabidopsis thaliana* genome was mined for gene products with physiologic stress and

apoptosis-relevant annotation. Mining was carried out using "The Arabidopsis Information Resource" and the Joint Genome Institute "Phytozome" framework, together with apoptosis-relevant information for these two organisms from GenBank (http://www.arabidopsis.org/; http://www.phytozome.net/). (Altschul, 1990; Merchant, 2007). Primers were designed *in silico* and optimized in vitro (see section 4.2.2.2) for the predicted PCD-relevant loci mined in the C. reinhardtii genome (Appendix A). Further *in silico* investigations revealed both interesting similarities and marked divergence in putative programmed cell death machinery, such as loci encoding putative Gene products mined from *A. thaliana* were used to build query sets to search for homologs in the *C. reinhardtii* genome. The *C. reinhardtii* genome was searched using BLAST (basic local alignment search tool) at a significance threshold of E-05 metacaspases, enzymes known to play central roles in programmed cell death processes (Figure 4-5) (Coll, 2010; Tsiatsiani, 2011). Amino acid sequences predicted for metacaspase genes in *Arabidopsis* and *Chlamydomonas* were aligned using ClustalX, and the guide tree for these pair-wise alignments is presented below (Larkin, 2007).

Early transcriptomic events associated with physiologic stress (125 mM) and PCD (250 mM) treatments were monitored *via* qPCR at 0, 1, 3 and 5 h. The results are summarized in Table 4.1. Certain instances of dramatic differential expression in PCD- and physiologic stress-response-relevant loci were evident (*e.g.*, metacaspase expression above and below controls in the PCD series of experiments), however, caveats must be applied in interpreting the information presented below, as inter-experiment variation was high (but intra-experimental standard deviation was low). The greatest increase in expression above controls was metacaspase (PCD, T=5), while the most dramatic downregulation was for also for the same gene at the initial sampling point just after experimental treatment (T=0). The magnitude of fold changes for the other genes (*i.e.*, HSP70, deg-P protease and Dad1a) was much less dramatic over the course of the PCD experiments; consistent with the hypothesis that metacaspase 1 is an apical regulator with tightly controlled expression. Under physiologic stress conditions, metacaspase also showed the greatest fold change above controls over each sampling point (Table 4.1). It is interesting to note that metacaspase expression levels appear relatively stable in these experiments, as those for HSP70 show upregulation over time. Data presented here were analyzed using the 2(-Delta Delta C(T)) method (Livak, 2001). Preliminary assessment of targeted expression data suggest the following: 1) Dramatic differential expression was suggested, accompanied by large inter-experiment variation, but modest intra-experimental deviation; 2) physiologic stress appears to be distinguishable from PCD from a magnitude of expression-difference perspective, with the most dramatic changes evident in metacaspase 1; 3) metacaspase expression increases dramatically over the PCD time course, but was relatively stable in the physiologic stress experiments; 4) expression trends for the other genes (HSP 70, Deg-P protease, Dad1a) were less clear, and appear to be less useful than metacaspase 1 for distinguishing physiologic stress *vs.* PCD.

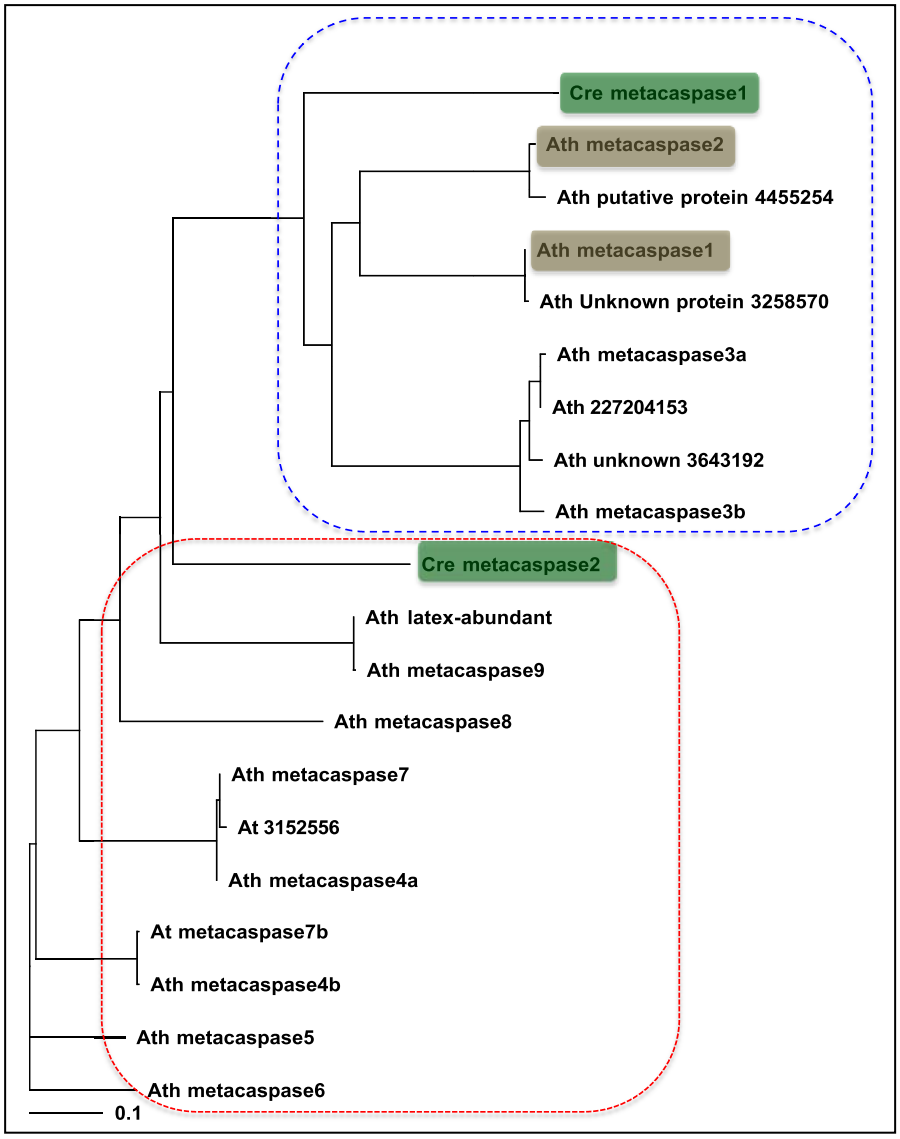

Figure 4.5 Estimated pair-wise distances among known and predicted metacaspase polypeptides in *A. thaliana* and *C reinhardtii*. Homology-based sequenced comparisons suggest two distinct functional cliques (red and blue circled clades) of of metacaspase-like proteases involved in programmed cell death (PCD) processes in *A. thaliana* and *C. reinhardtii.* In *A. thaliana*, two type 1 metacaspases (AtMC1, AtMC2; highlighted in brown) antagonistically control programmed cell death; *At*MC1 positively regulates the process, while *At*MC2 is a negative regulator. The other metacaspase-related proteins in *Arabidopsis* have not yet been the focus of detailed molecular and genetic analyses, nor have the two predicted polypeptides in *Chlamydomonas* (highlighted in green).

Table 4.1 Differential Expression of Programmed Cell Death- and Physiologic Stress-Relevant Loci

	Metacaspase	HSP70	Deg-P	Dad1a
PCD T =0	-139.22 ± 248.56	-1.5 ± 2.85	-4.64 ± 3.42	-2.8 ± 0.64
PCD T= 1	1.51 ± 3.55	-1.25 ± 2.26	0.38 ± 4.42	-10.7 ± 16.56
PCD T=3	-10.26 ± 8.23	-1.6 ± 3.03	-17.57 ± 13.86	-7.68 ± 7.12
PCD T=5	25.05 ± 40.67	1.04 ± 2.87	-0.49 ± 1.33	0.29 ± 1.59
Stress T=0	3.45 ± 2.79	-3.37 ± 2.57	-2.52 ± 1.32	-4.22 ± 1.96
Stress T=1	5.89 ± 1.03	2.67 ± 0.01	-0.25 ± 1.79	-0.09 ± 1.58
Stress T=3	-4.85 ± 4.57	-0.83 ± 4.17	-16.94 ± 14.16	-8.37 ± 9.89
Stress T=5	4.10 ± 3.64	0.49 ± 2.23	-2.40 ± 1.32	-2.34 ± 1.2

4.4. Conclusions and Future Outlook

Results presented here highlight molecular events and processes potentially useful in monitoring algal pond health and stability. Early, middle and late multi-dimensional samplings of *C. reinhardtii* cells under physiologic stress (150 mM) and PCD-inducing (250 mM) conditions are distinguishable (Figures 4.1 – 4.4), and in certain instances, suggest thresholds beyond which cultures will not recover if in programmed cell death molecular mode (*e.g.*, Figures 4.2 and 4.3)

Follow-on work will include genome-wide responses to the PCD treatment. RNASeq experiments will be performed at the initial and three hour time points for control and 250 mM NaCl treatment sample sets, containing two biological replicates each. Multiplex-sequencing on an Illumina platform will be used; single-end 50 base reads will be obtained for each replicate. Libraries and sequencing will be performed at National Center for Genome Resources in collaboration with Dr. Joann Mudge and colleagues. Data will be analyzed using SNL and NCGR bioinformatics resources and expertise. Genome-wide expression patterns will be validated using our quantitative polymerase chain reaction (qPCR) results.

5. IDENTIFICATION OF FLUORESCENCE SPECTRAL SIGNATURES FOR ALGAL GROWTH AND PRODUCTIVITY AT THE SUBCELLULAR, SINGLE CELL AND ENSEMBLE LEVELS

5.1. Introduction

Fluorescence hyperspectral imaging has been an ideal tool for characterizing photosynthetic pigments in plants, cyanobacteria and algae (Davis, 2012; Pedroso, 2010; Ruffing, 2012; Vermaas, 2008). With the use of Sandia's hyperspectral confocal fluorescence microscope plus Sandia's image analysis algorithms, we were able to discover independently varying spectral signatures without any prior knowledge about the algal sample being imaged. This ability allowed us to discover endogenous fluorescence signatures that were associated with the algae and how these signatures changed depending on the condition of the algal cells (e.g., health or stress). In addition, imaging provided the location of these signatures at the cellular and subcellular level which aided in the interpretation of how the algal cells were changing as a result of the environment or experimental conditions. Once these spectral signatures are obtained, they can be utilized for monitoring algal cells in pond and raceways using a simpler bulk or ensemble fluorescence measurement. In this report, we will only discuss the spectral signatures that have been found to give information about the health and state of the algae. Future work can build upon these signatures to generate monitoring technologies. Hyperspectral confocal fluorescence microscopy is used for characterization in other sections of this report; therefore this section gives a brief overview of the instrumentation and the preprocessing and analysis techniques used globally throughout the project.

5.2. Hyperspectral Confocal Fluorescence Microscopy

5.2.1 Instrumentation

This project utilized a hyperspectral confocal fluorescence microscope developed at Sandia (Sinclair, 2006). This microscope is equipped with multiple objectives (10x, 20x, and 60x). For the experiments conducted in this report, only a Nikon 60x oil immersion objective (NA 1.4 plan apochromat) was used. This provided a 25 x 25 micron square field of view for all of the images with diffraction limited spatial resolution. The microscope is also equipped with a solid state 488 nm laser (Coherent, Incorporated). This excitation source was utilized for all imaging, except for the two-photon imaging discussed in section 5.3. If required for the experiment, an emission filter (Newport Optics, BG-38) was placed prior to the EMCCD to reduce the chlorophyll emission and allow us to increase the laser power by a factor of 300. This increased power allowed us to obtain resonance enhanced Raman spectral signatures of the carotenoid pigments in algae, while preventing the saturation of the EMCCD with the chlorophyll emission.

5.2.2. Data preprocessing and analysis

The image datasets were preprocessed to remove unwanted spectral artifacts present in the hyperspectral images. These artifacts consisted of cosmic gamma-ray spikes, detector offset, and a structured noise artifact. These preprocessing techniques are extensively described by Jones et al. (Jones, 2012). After preprocessing data, the data were analyzed using Multivariate Curve Resolution (MCR) algorithms using Sandia developed image analysis software packages (imageMCR© and rapidMCR©). Overlapping fluorophores are typically problematic for many

traditional fluorescence microscopy techniques; however hyperspectral imaging allows for the separation of many overlapping fluorescence species and creates interpretable quantitative images from biological samples with both known and unknown fluorescence species. MCR provides a relative quantitative analysis of the hyperspectral image data without the need for standards, and it discovers all the emitting species present in an image, even those in which there is no *a priori* information (Collins, 2011; Haaland, 2009; Timlin, 2005). MCR requires that the emitting species vary independently, therefore (when possible) to improve the separation of the spectral signatures, the hyperspectral images were combined and analyzed together from multiple images within the experiment of interest, thereby maximizing the differences in the spectral signatures.

5.3. Characterization of Microalgae using Two-photon Excitation Hyperspectral Imaging

Two-photon excitation hyperspectral imaging was used as a tool to understand and extract spectral signatures associated with the health of algal cultures. The use of a tunable Chameleon-Ultra pulsed laser (Coherent, Inc.) allowed for the exploration of multiple excitation wavelengths varying from 690 to 1040 nm on the same algal sample. Since the emission intensity of each spectral species is dependent on the excitation wavelength, multiple excitations will cause the relative intensities of each spectral species to vary in independent from each other, thereby improving the MCR analysis and improving the estimate of the overall spectral signature.

5.3.1. Experiment

C. reinhardtii cells were grown photoheterotrophically for 7 days. The cells were then subject to heat treatments to create three different cell conditions: 1) unheated cells (healthy control), 2) cells incubated at 55 degrees C for 10 minutes (PCD-like cells), and 3) cells incubated at 85 degrees C for 2 minutes (necrotic cells). Figure 5-1 shows optical light microscopy of the morphological changes between the three different cell conditions. Cells were then immobilized onto 0.75% agar coated slides and the samples were sealed using a coverslip and fingernail polish.

Hyperspectral images were taken at each condition using three different two-photon excitation wavelengths (750, 840 and 976 nm). These wavelengths were selected based upon the single photon excitation wavelengths of 375, 420 and 488 nm. The emission wavelengths (490-740 nm) were collected on the EMCCD for each of the excitations. To prevent stray reflections of the laser at the detector, a cut-off filter was used to block emissions starting at 740 nm. We collected 12 confocal sections of *C. reinhardtii* from the three different cell conditions (3 sections of the healthy control, 4 sections of the "PCD-like" condition, and 5 sections of the necrotic condition). The emission of each confocal section was repeated at the three different excitations (750, 840 and 976 nm) to create 36 total images.

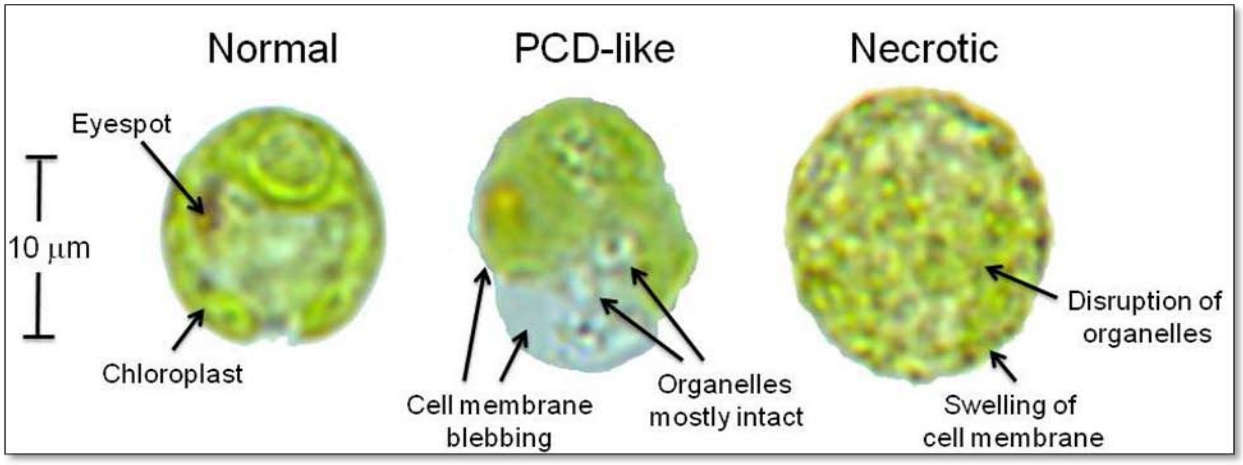

Figure 5-1: Optical microscopy captures the morphological effect of heat stress on C. *reinhardtii*.

5.3.2. Data analysis

All 36 images from the three different cell conditions and three different excitation wavelengths were combined together for the MCR analysis. The initial MCR analysis discovered four spectral components that we interpret to be: 1) Antenna chlorophyll that is a combination of chlorophyll *a* and chlorophyll *b* but is denoted chlorophyll *b* for clarity, 2) Photosystem I (PSI), 3) Chlorophyll *a*, and 4) a chlorophyll shift related to antenna chlorophyll. Normally, we apply non-negativity constraints to prevent the spectral components and the resulting concentrations (or intensities) from being negative; however in some cases it's necessary to remove this constraint (Haaland, 2009). In this analysis, it was necessary remove this constraint to model a varying shift in the chlorophyll. Figure 5-2 shows these four spectral components. Figure 5-3 shows the relative intensities of the chlorophyll *b* (green), chlorophyll *a* (red) and PS I (blue) components represented as RGB images for the 750 nm excitation images. Figure 5-4 shows the concentration images for the chlorophyll shift component.

5.3.3. Results

These results will focus on the comparison of the images from the single excitation wavelength of 750 nm. Although the results are slightly different across the images for the other two excitation wavelengths, the same general conclusions apply. The relative intensities of the pigments change across conditions as observed in Figure 5-3. The relative intensity of the PSI component increases in intensity relative to the two chlorophyll components as the cells become increasingly stressed. Figure 5-5 shows the percent relative distributions of the pigments per cell condition and per excitation wavelength. For the healthy cells, chlorophyll *b* is the most intense because the cells are energy transfer limited. However, as the cells become stressed, these energy transfer pathways begin to degrade and therefore the pigment distributions begin to change. The degraded pathways no longer dictate the relative intensities of the pigments; instead the excitation wavelength dictates the intensity. As can be seen with the necrotic cells, each excitation wavelength has a different relative distribution of pigment intensities. Curiously, the amount of chlorophyll shift is more dominate in the "PCD-like" stressed cells as compared to the healthy or necrotic cells (Figure 5-4). This shift component can be used as an early health indicator of stressed cells. Overall, this type of imaging provided insights into the energy

transfer mechanism of the cells undergoing heat stress, as well as provided a spectral biomarker for cell status.

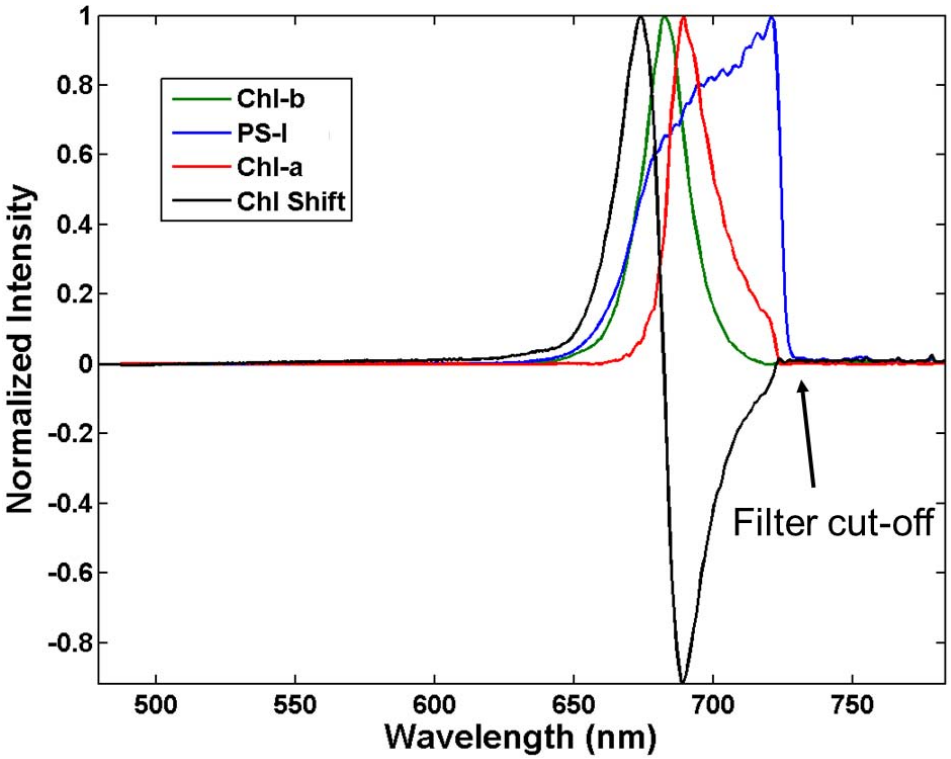

Figure 5-2: MCR pure spectral components

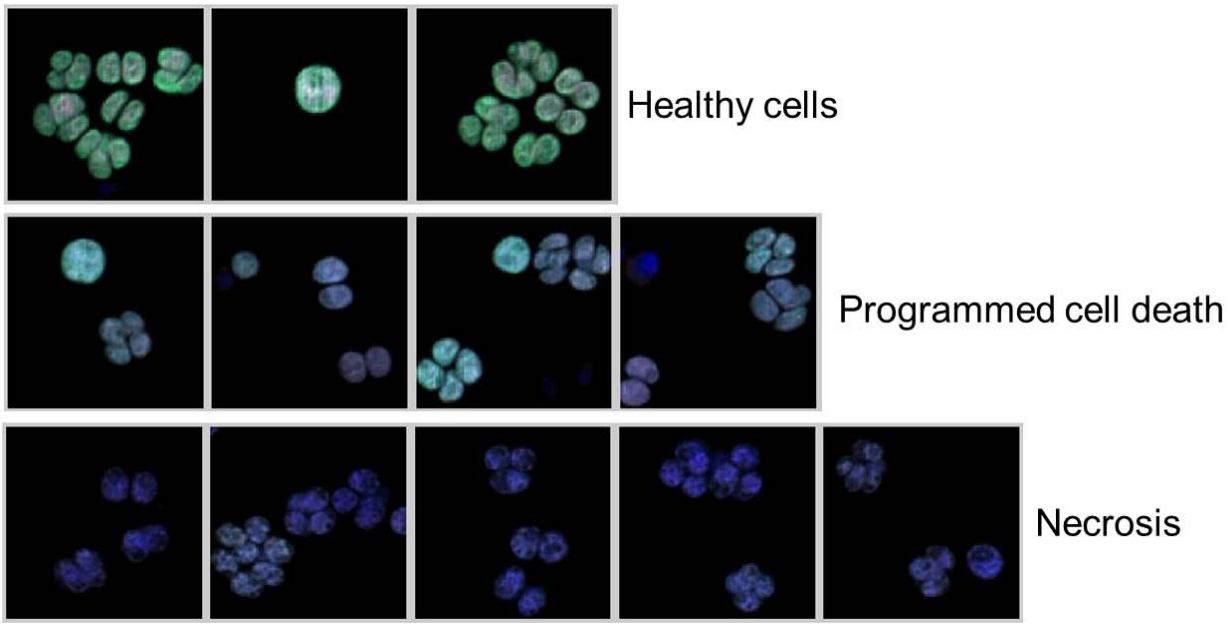

Figure 5-3: Emission images from the 750 nm excitation are shown. The colors of these RGB images represent the colors from the spectral components in Figure 5-2.

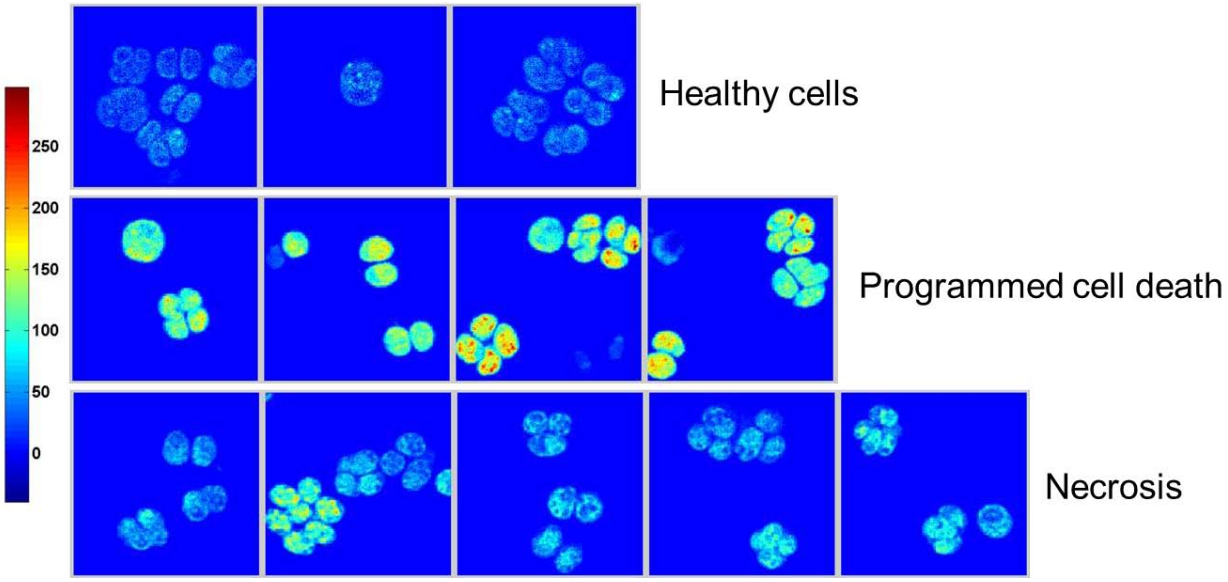

Figure 5-4: Concentration images of the chlorophyll shift from the 750 nm excitation are shown.

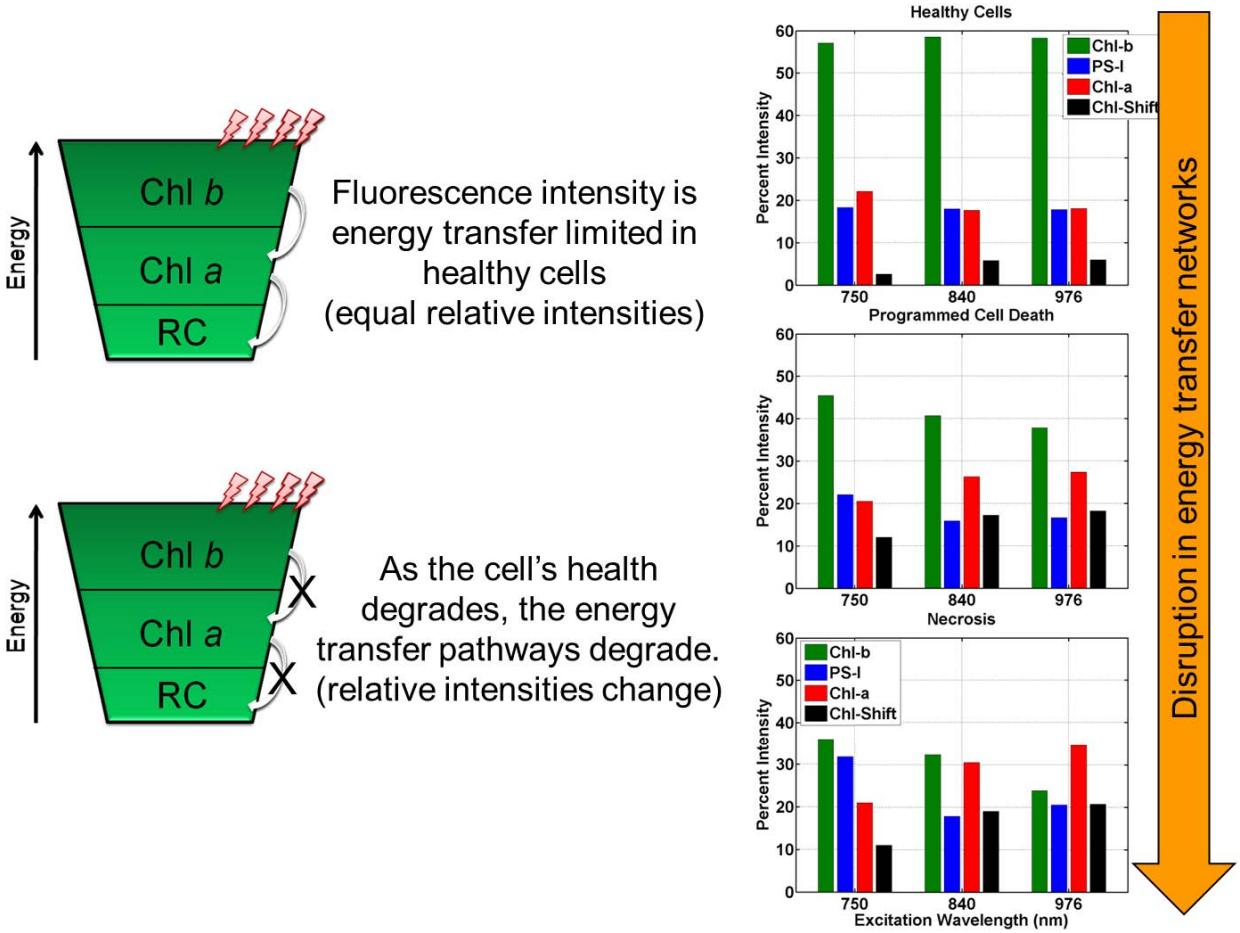

Figure 5-5: Percent distribution of pigment intensity for each cell condition for each excitation wavelength. Under optimal conditions cells are energy transfer limited, however as the cells become stressed the energy pathways begin to degrade.

5.4. Hyperspectral Imaging Results from Greenhouse Algae Study

Hyperspectral imaging was used to understand the spectral signatures associated with algae in a non-laboratory setting. We conducted greenhouse studies to temporally follow the health of two algal ponds by changing the CO_2 concentration and as a consequence, the pH of the ponds. Finally, the ponds were intentionally crashed to understand whether spectral signatures can provide early warnings into the health-status of the ponds.

5.4.1. Experiment

A laboratory grown culture of *N. salina* were inoculated into two ponds (west and east) at the greenhouse located at Sandia in Tech Area III. These ponds are briefly described and shown in section 2 of this report. The experiment consisted of measuring the two ponds during a two-week period of time in November 2011. The two ponds were operated at different CO_2 levels. The first week, the west pond was bubbled at 3 scfh CO_2, while the east pond only had ambient CO_2 levels. The second week the CO_2 levels were swapped for the two ponds. Following this two week experiment, the ponds were crashed with the use ~0.005% (v/v) sodium hypochlorite.

Fluorescence hyperspectral imaging using single photon 488 nm laser excitation was performed on aliquots of samples acquired from each pond. These measurements occurred at four different times of the experiment: 1) After the first week, 2) After the second week, 3) Following day 1 of bleach addition, and 4) Following day 2 of bleach addition. Samples were prepared onto glass slides and sealed with a coverslip and fingernail polish. Data were collected with and without the BG-38 emission filter to obtain both carotenoid and chlorophyll only data sets.

5.4.2. Data analysis

After the preprocessing of the data, the chlorophyll only and carotenoid data sets were combined and analyzed separately using MCR. Following MCR to obtain the spectral components and the associated intensities for each component, the mean intensities of each cell for each spectral component was calculated using an in-house written Matlab routine called CellFinder (Collins, 2012). Temporal trends between the spectral components were observed by looking at multidimensional plots, also created using Matlab.

5.4.3. Results

Figure 5-6 shows the spectral components obtained using MCR for the chlorophyll only region. Since *N. salina* only has chlorophyll *a*, this was the major component found within the cells. As indicated in section 5.3, it is necessary to remove the non-negativity constraints when modeling spectral shifts. It is also true for modeling spectral broadenings. Spectral shifts can be modeled with the use of a derivative while a spectral broadening can be modeled with the use of a 2nd derivative. We found both a shift and a broadening spectral component associated with chlorophyll *a* in this pond study. For this chlorophyll only model, there were only 3 components. Representative images are also shown in Figure 5-6, the colors of these RGB images correspond to the colors of the spectral components (chlorophyll *a* is green, the shift is red and the broadening is blue). The images become bluer over the two week course of the experiment. This can be more easily seen in the three-dimensional scatterplot. As the cells become older over the course of this experiment, the intensity of chlorophyll *a* decreases and the

signature broadens. However, during the pond crash, as highlighted in Figure 5-6, the spectral signature of chlorophyll *a* significantly decreases, broadens and red-shifts. For clarity, only the west pond is shown in the scatterplot, although the east pond shows the same trend. In conclusion, small subtle changes in the chlorophyll signature can differentiate unhealthy cells that can be used for early detection of algal health problems.

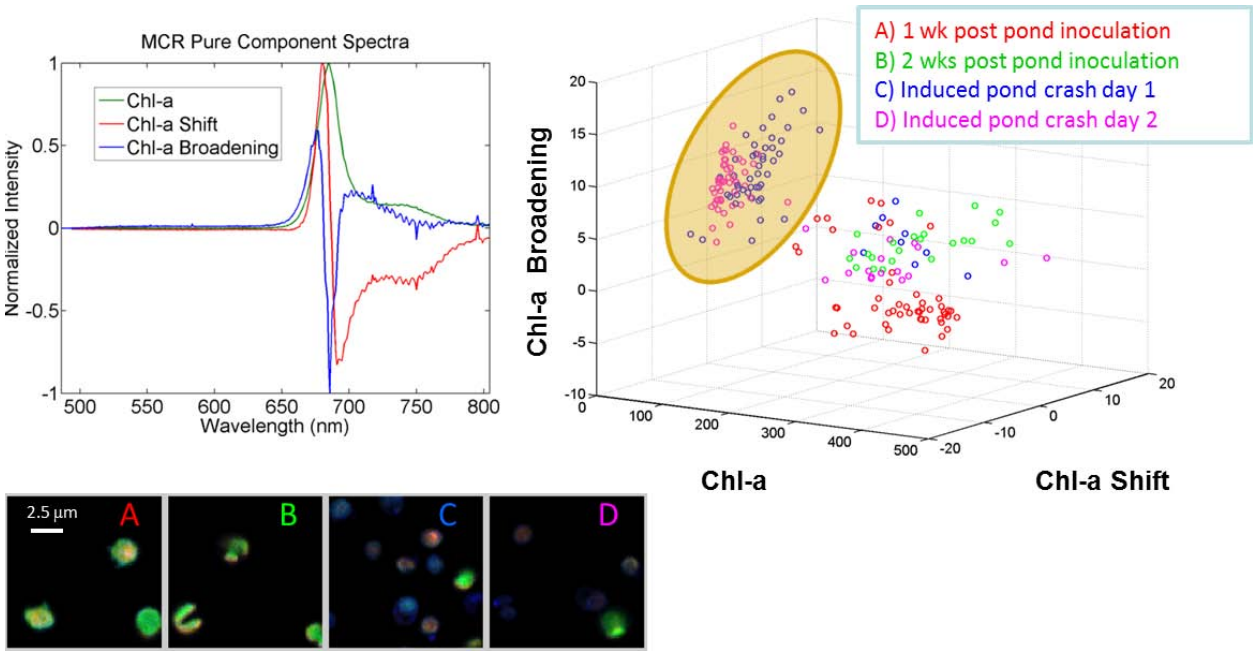

Figure 5-6: Chlorophyll only imaging results from greenhouse CO_2 study. (Top Left) Small spectral variations (shift, broadening) found in the chlorophyll signature of *N. salina*. (Right) Scatter plot of the 3 discovered spectral signatures. Chlorophyll intensity alone is independent of cell health, however chlorophyll intensity + amount of chlorophyll broadening can be used an indicator of cell health. (Bottom Left) RGB images from the four cell populations shown in the scatter plot. RGB colors correspond to the pure component spectra.

Figure 5-7 shows the spectral components obtained using MCR for the carotenoid spectral region. For this spectral region, MCR discovered four spectral components. Building upon the work from a previously internally fund program ("From Algae to Oilgae: in-situ Studies of Factors Controlling Growth and Oil Production", Sand Report, submitted September 28, 2011, SAND2011-7241), we were able to use carotenoid as a spectral marker for lipid within the *N. salina* cells. The red spectral component is a carotenoid spectral signature specific to lipid within the algal cells. The sharp spikes are the resonance-enhanced Raman bands associated with carotenoids. The green spectral component also has carotenoid features and is associated with the chloroplast. Its fluorescence shape is different from the lipid carotenoid shape and the resonance enhanced Raman bands have different relative intensities compared to the lipid carotenoid spectral signature. Due to these differences, we are able to differentiate the lipid from the chloroplast solely upon the differences in the carotenoid signature. Also, since the emission filter does not entirely block the chlorophyll emission and chlorophyll *a* co-varies with the carotenoid present in the chloroplast, it is extracted as one spectral component. In addition, there is a broad auto-fluorescence component that is specifically associated with the health of the cells. Also shown in figure 5-7 are representative hyperspectral images acquired. The colors of these

images correspond to the spectral component colors (green = chloroplast, red = lipid, and blue is autofluoresence). Notic e the lipid droplets in red compared to the green chloroplast (the cell membrane is not visible in fluorescence without the use of an exogenous fluorophore). When the pond crashes, the spe ctral signature becomes dominated by only the auto-fluorescence component. The scatterplot shown in Figure 5-7 illustrates the ability to track an external pond with respect to lipid production and the health of the cells. Week 1 (red points) shows the cells healthy with increased chlorophyll. Week 2 (green points) shows cells becoming stressed (lower chlorophyll), however the lipid production has increased. Af ter the induced pond c rash, the majority of the cells fall in the upper right hand quadrant with an increase and dominance in the autofluorescence. In conclusion, these three spectral biomarkers can be used to describe two of the most important parameters in algae farming: 1) lipid production rates and 2) health of the pond or raceway.

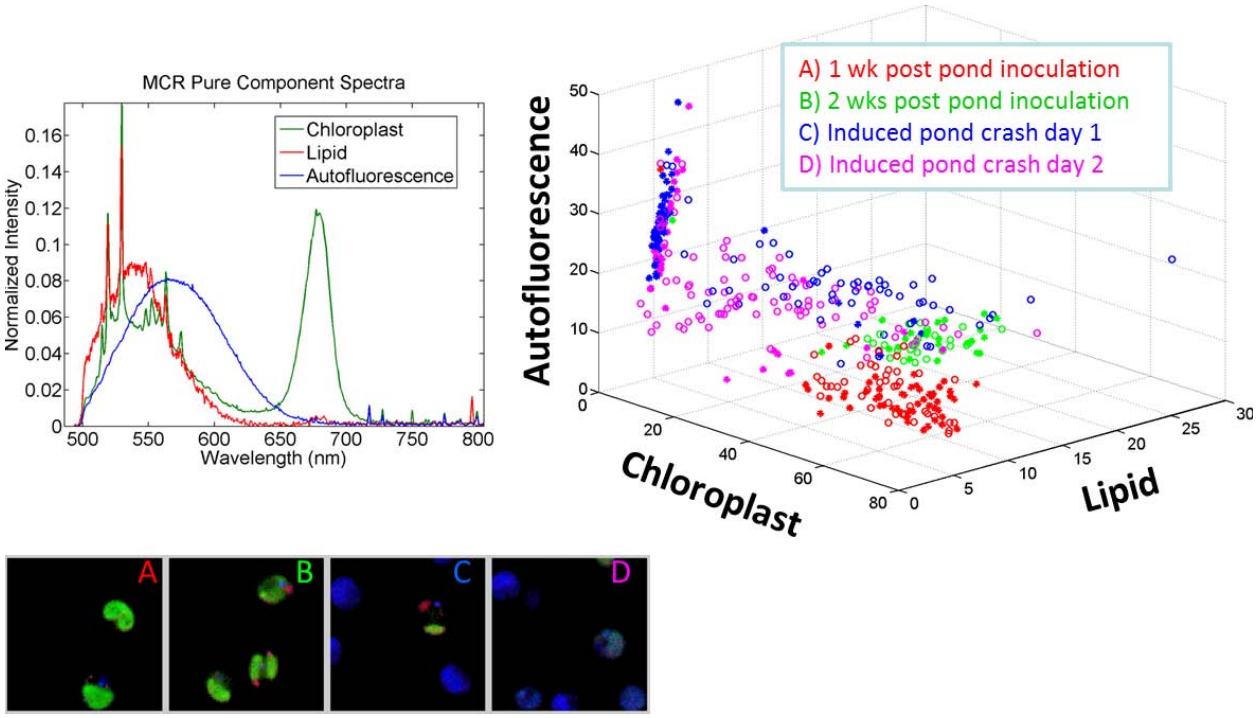

Figure 5-7: Carotenoid imaging results from greenhouse CO_2 study. (Top Left) Three spectral components representing the chloroplast, lipid and an autofluorescence component in *N. salina*. (Right) Scatter plot of the 3 discovered spectral signatures (* - west pond, o – east pond). The autofluorescence intensity is an indicator of cell health. These signatures can be used for the development of methodologies to monitor ponds for health and lipid content. (Bottom Left) RGB images from the four cell populations shown in the scatter plot. RGB colors correspond to the pure component spectra.

5.4.4. Carotenoid characterization studies

It should be pointed out that we have looked extensively at the resonance enhanced Raman spectral signatures using hyperspectral Raman microscopy (Collins, 2011) rather than the fluorescence hyperspectral imaging described above during this project. These published findings showed that w e could extract multiple carotenoid species and isolate these species within live algal cells.

5.5. Conclusions and Future Outlook

Although the findings described in this section require rather sophisticated instrumentation and analysis algorithms to develop endogenous spectral biomarkers that are important to algal biofuels, the spectral biomarkers found can later be used for the development of less sophisticated spectroscopic monitoring methodologies for ponds and raceways. One example can be the use of a flow-cell that is continually sampling an algal pond and recording the fluorescence signatures to monitor the status of the algae and lipid production. Spectroscopic monitoring can be an early indicator of a change in pond status and signal the need for additional off-line measurements.

6. DEVELOPMENT AND OPTIMIZATION OF COMPUTATIONAL FLUID DYNAMICS MODELS OF ALGAL GROWTH AND PRODUCTIVITY

6.1. Introduction

Despite their lower specific yield when compared to closed photobioreactors, open ponds, particularly raceway style ponds, are typically used for large-scale algae cultivation due to the lower cost to build, operate, and maintain them. Thus it is especially important to optimize these systems. A number of operational parameters are candidates for analysis and optimization, including temperatures, incident radiation, effects of covering raceways with greenhouses, nutrient distribution and availability, depth flow characteristics, geometry and channel dimensions, and predation.

Models and numerical simulations are relatively inexpensive tools that can be used to enhance economic competitiveness through operation and system optimization to minimize energy and resource consumption while maximizing algal oil yield. This work uses modified versions of the U.S. Environmental Protection Agency's Environmental Fluid Dynamics Code (EFDC) (Thanh, 2008) in conjunction with the U.S. Army Corp of Engineers' water-quality code (CE-QUAL)(Cerco, 1995) to simulate flow hydrodynamics coupled to algal growth kinetics(James, 2010). The model allows the flexibility of manipulating a host of variables associated with algal growth such as temperature, light intensity, and nutrient availability.

6.1.1. Growth kinetics model

The governing equation for biomass growth in CE-QUAL is (Cerco, 1995):

$$\frac{\partial B}{\partial t} = (P - B_M - P_R)B + \frac{\partial}{\partial z}(w_s B) + \frac{B_L}{V}, \tag{6.1}$$

where B (g/m^3 or mg/L) is the biomass, t (days) is time, P (day^{-1}) is the production (growth) rate, B_M (day^{-1}) is the basal metabolic rate, P_R (day^{-1}) is the predation rate, w_s (m/day) is the settling velocity, z (m) is the vertical coordinate, B_L (g/day) represent external loading rates from inoculation and harvesting, and V (m^3) is the model cell volume. Biomass production rates are determined by the availability of nutrients (including CO_2), light intensity, local temperature, and pH. The effect of each is multiplicative and decoupled (Cerco, 1995),

$$P = P_M f(n) g(I) h(T) i(\text{pH}). \tag{6.2}$$

where, P_M (day^{-1}) is the maximum production rate under optimal conditions, $f(n)$ is the effect of non-optimal nutrients, which includes CO_2 limitation ($0 \le f(n) \le 1$), $g(I)$ is the effect of non-optimal illumination ($0 \le g(I) \le 1$), $h(T)$ is the effect of non-optimal temperature ($0 \le h(T) \le 1$), and i(pH) is the effect of non-optimal pH ($0 \le i(\text{pH}) \le 1$). All of these functions are spatially dependent, and their values vary from cell to cell in the model according to local nutrient concentrations (including CO_2), incident solar radiation, and temperature. (Cerco, 1995)

6.1.2. Growth model improvements

The pH of the medium is a newly added operational parameter governing algal growth that affects algae photosynthesis, differential availability of inorganic forms of carbon, enzyme activity in algae cell walls, and oil production rates. (Janardhanam, 2012) Media pH can be entered as a measured value or calculated based on CO_2 concentrations.

The first step toward optimizing such a system is achieving an in-depth understanding of which parameters play significant roles in affecting the rate at which biomass is produced (i.e., a sensitivity study). Once sensitive variables have been identified, not only can they be optimized (e.g., water-column depth), but modelers can request that experimentalists collect specific data (e.g., concentration dependent light attenuation) to help reduce model uncertainties. In this work, a sensitivity study is performed in which the roles of chlorophyll-based light extinction, water-column depth, production rate, and basal metabolic rates are examined.

6.2. Incorporating Algal Growth Dependency on pH

Inorganic carbon plays an important role in eutrophication processes and is available in several forms in water: free dissolved CO_2, carbonic acid (H_2CO_3), bicarbonates (HCO_3^-), and as carbonates (CO_3^{2-}). The relative amount of each form of carbon present in the media is closely related to the pH of the media. At pH values less than 6.5, the dominant form of inorganic carbon in the medium is free CO_2, while at pH values above 10, inorganic carbon mostly exists as carbonates. Between pH values of 6.5 and 10, bicarbonates form the major source of inorganic carbon. For photosynthesis, all algae species use free dissolved CO_2 although many also use bicarbonates and some species can use carbonates and can grow in high-pH environments (e.g., *Scenedesmus quadricauda*). It is also known that carbonate ions can be toxic to certain algae species and hence elevated pH can lead to species succession and competition (Hansen, 2002). Because pH has an intrinsic effect on enzymes in algae cell membranes and walls, which are responsible for absorption of different essential nutrients, pH affects photosynthesis (Moss, 1973). High extracellular pH can also alter membrane transport processes and change the cellular content of amino acids and their relative compositions and hence affect growth rates (Raven, 1980; Smith, 1979). Moreover, pH of the medium is also known to influence biomass regulation and even metabolic rates of certain algae species (Azov, 1982; Goldman, 1982). Clearly, pH is an important factor for algae growth and must be considered in a growth model. pH limitation is represented with a decoupled multiplicative function, i(pH); this is included along with other factors (i.e., light, temperature, nutrients) to limit the production rate for an algal group in Equation 6-2.

To simulate the effects of pH limitation, the maximum and minimum values of pH that support algae growth must be estimated. If pH of the medium is elevated, then growth may be inhibited in most species due to the lack of free dissolved CO_2. Most algae species can maintain growth up to pH values of 8.6−8.85. Some species that can get CO_2 from bicarbonates or carbonates can grow up to pH values of 9.2−9.3 Most algae species do not grow well below pH values of 4.5−5.1, although certain species (e.g., *Euglena gracilis*) can grow in pH values at least as low as 3.9 (Moss, 1973). In many practical instances, CO_2 concentrations may not be known, but pH is often measured. The model is set up to handle pH as a data input or to calculate i(pH) based on CO_2 concentrations (if these are known or can be calculated based on CO_2 concentrations). pH

also varies with temperature, however only by 0.1 unit per 20°C change in temperature so this effect is ignored here.

6.2.1. pH limitation with known pH values

With known pH, the multiplicative function $i(\mathrm{pH}) \sim i([\mathrm{H}^+])$ is modeled after the work of Mayo (1997),

$$[\mathrm{H}^+] = 10^{(-\mathrm{pH})}$$
$$i([\mathrm{H}^+]) = \frac{[\mathrm{H}^+]}{[\mathrm{H}^+] + k_{\mathrm{OH}}(T) + [\mathrm{H}^+]^2 / k_{\mathrm{H}}(T)}. \tag{6.3}$$

where the hydration constants are modeled as a function of temperature (°C), which is obtained from a polynomial fit to data available from Mayo (1997),

$$\begin{aligned} k_{\mathrm{OH}}(T) &= 10^{-13}\left(8T^2 - 500T + 8000\right), \\ k_{\mathrm{H}}(T) &= 10^{-7}\left(-5T^3 + 300T^2 - 5000T + 30000\right). \end{aligned} \tag{6.4}$$

6.2.2. pH calculated from CO_2

At the air-water interface (especially if CO_2 is bubbled through the growth medium), the interaction between H_2O and CO_2 results in formation of carbonic acid (H_2CO_3) that dissociates into two protons (H^+) and a carbonate (CO_3^{2-}). Thus, all else being equal, an increase in CO_2 results in a decrease in the media pH; this can be directly evaluated. The functional form of the relation between pH and dissolved CO_2 is derived from chemical equilibrium theory.

Gaseous CO_2 ($CO_{2(g)}$) upon contact with H_2O becomes aqueous CO_2 ($CO_{2(aq)}$), which in turn reacts with H_2O to form carbonic acid:

$$\begin{aligned} \mathrm{CO}_{2(g)} + \mathrm{H}_2\mathrm{O} &\leftrightarrow \mathrm{CO}_{2(aq)} + \mathrm{H}_2\mathrm{O}, \\ \mathrm{CO}_{2(aq)} + \mathrm{H}_2\mathrm{O} &\leftrightarrow \mathrm{H}_2\mathrm{CO}_3. \end{aligned} \tag{6.5}$$

In the preceding reactions, only a small fraction of $CO_{2(aq)}$ is converted into H_2CO_3, which is given by the hydration constant (at 25°C) as

$$k_{\mathrm{h}} = \frac{[\mathrm{H}_2\mathrm{CO}_3]}{[\mathrm{CO}_{2(aq)}]} = 1.7 \times 10^{-3}. \tag{6.6}$$

H_2CO_3 is a diprotic acid that can dissociate into two protons in a two-stage process:

$$\begin{aligned} \mathrm{H}_2\mathrm{CO}_3 &\overset{k_1}{\leftrightarrow} \mathrm{H}^+ + \mathrm{HCO}_3^-, \\ \mathrm{HCO}_3^- &\overset{k_2}{\leftrightarrow} \mathrm{H}^+ + \mathrm{CO}_3^{2-}, \end{aligned} \tag{6.7}$$

with dissociation (or acidity) constants for the two stages of:

$$k_1 = \frac{[\mathrm{H}^+][\mathrm{HCO}_3^-]}{[\mathrm{H}_2\mathrm{CO}_3]} = 4.45 \times 10^{-7}, \tag{6.8}$$

$$k_2 = \frac{[\mathrm{H}^+][\mathrm{CO}_3^{2-}]}{[\mathrm{HCO}_3^-]} = 4.69 \times 10^{-11}. \tag{6.9}$$

Because $k_1 >> k_2$, the second stage o f dissociation proceeds slowly and can be neglected. Under this assumption, carbonic acid is considered a weak monoprotic acid.

The initial concentration of H_2CO_3 dissociates into carbonates and bicarbonates, thus mass balance provides the net concentration of dissolved CO_2 (note that these equations show concentration equivalence, not stoichiometric equivalence):

$$k_h[CO_2] = [H_2CO_3]_{initial} = [H_2CO_3] + [HCO_3^-] + [CO_3^{2-}], \quad (6.10)$$

and from the electro-neutrality condition,

$$[H^+] = [OH^-] + [HCO_3^-] + 2[CO_3^{2-}]. \quad (6.11)$$

Under the assumption that carbonic acid is a weak monoprotic acid, $[CO_3^{2-}]$ formed during the second dissociation of $[HCO_3^-]$ is neglected.

From the preceding two equations, $[HCO_3^-]$ and $[H_2CO_3]$ concentrations are:

$$[HCO_3^-] = [H^+] - [OH^-] \quad (6.12)$$

$$[H_2CO_3] = k_h[CO_2] - [HCO_3^-] = k_h[CO_2] - [H^+] + [OH^-], \quad (6.13)$$

and these are substituted into Equation 6-8 to calculate k_1

$$k_1 = \frac{[H^+]([H^+] - [OH^-])}{k_h[CO_2] - [H^+] + [OH^-]}. \quad (6.14)$$

Using the hydration constant for water, $k_w = [H^+][OH^-] = 1.008\times10^{-14}$ at 25°C, and using $[OH^-] = k_w/[H^+]$, the simplified expression for k_1 in terms of $[H^+]$ is

$$[H^+]^3 + k_1[H^+]^2 - (k_1k_h[CO_2] + k_w)[H^+] - k_1k_w = 0. \quad (6.15)$$

This is a cubic equation in $[H^+]$ that can be solved numerically and depends on the parameters k_1, k_w, and $[CO_2]$, all of which are known. However, in the preceding equation, k_1k_w is negligible; $\sim O(10^{-21})$, so it can be reduced to a quadratic. Rearranging Equation 6-15 yields,

$$[H^+]^2 + k_1[H^+] - (k_1k_h[CO_2] + k_w) = 0. \quad (6.16)$$

From Equation 6-16, the quadratic equation yields

$$\begin{aligned} [H^+] &= \frac{-k_1 + \sqrt{k_1^2 + 4(k_1k_h[CO_2] + k_w)}}{2}, \\ [H^+] &\approx \frac{-k_1 + \sqrt{4(k_1k_h[CO_2] + k_w)}}{2} = -\frac{k_1}{2} + (k_1k_h[CO_2] + k_w)^{\frac{1}{2}} \approx (k_1k_h[CO_2] + k_w)^{\frac{1}{2}}. \end{aligned} \quad (6.17)$$

Note that above approximations yield a simple expression for pH as a function of $[CO_2]$:

$$\begin{aligned} [H^+] &= (k_w + k_1k_h[CO_2])^{\frac{1}{2}}, \\ pH &= -\log_{10}([H^+]) = -\frac{1}{2}\log_{10}(k_w + k_1k_h[CO_2]). \end{aligned} \quad (6.18)$$

The preceding expression for pH was calculated assuming that k_2 is negligible. In a more precise scenario, k_2 could be considered and a thorough analysis of the chemical equilibrium theory in the presence of bicarbonates and carbonates could be used (Park, 1969). Of course, other chemical factors not considered here could yield changes in pH and increased alkalinity, so it may be best to simply measure pH for use in the limitation function, i(pH).

6.3. Assessing the Sensitivity of Algal Growth Model to Input Parameters

Different algal strains have different growth rates, different metabolic rates, different settling rates, require different nutrients, exhibit different self-shading properties, and attract different types of grazers. Biomass production does share qualitative properties across systems. For example, biomass production always ceases in the absence of light or nutrients, grazers always cause biomass to decrease, reproduction always causes biomass to increase, and self-shading always reduces the available down gradient light energy. To understand the behavior of a wide variety of algae systems, SNL-EFDC is supplied with a physically realizable range of parameter values and the sensitivity of the overall biomass to the parameters is observed. In particular, the parameters to be investigated are chlorophyll-based light extinction k_{Chl}, water-column depth d, maximum production rate PM_{x}, and decay rate S (the rate at which biomass decreases due to respiration and grazing). Throughout the analysis, nutrients are assumed to be in abundance.

The system's final biomass is independent of the initial concentration and that for a given system (i.e., set of parameter values) the biomass concentration approaches a constant value; this is its *carrying capacity*, B^*. However, the carrying capacity is dependent upon the parameter values. Therefore, the problem of biomass optimization reduces to determining the parameter values that yield the largest carrying capacity.

For example, to determine the way in which depth affects B^*, all of the other parameters are set to their base values and B^* is numerically for various values of d. The scaled sensitivity of parameter p is given by $p\left|\partial B^* / \partial p\right|$, with all other parameters held at their base values. Sensitivity plots in Figure 6.1 are constructed by differentiating the single-variant curves normalizing the parameters across their ranges using the transformation

$$p, B^* \rightarrow \left(\frac{p - p_{\min}}{p_{\max} - p_{\min}}, p\left|\frac{\partial B^*}{\partial p}\right| \right). \tag{6.19}$$

From this plot, it is clear that all parameters are sensitive at some point in their range. For predictive models, these parameters will have to be measured precisely to ensure agreement with the physical system, especially where sensitivities are greatest.

Figure shows how *individual* parameters may be optimized, but, in practice, it is unlikely that these parameters will be optimized individually. Rather, they are optimized cumulatively, meaning that their *combination* will be optimized. To do this, a quantitative relationship is required between B^* and d, k_{Chl}, S, and PM.
The general relation is

$$B^* \approx \frac{r_{\mathrm{CChl}}\left(e \times PM - PM \times e^{1 - I_0/I_s} - SdK_{\mathrm{b}}\right)}{Sdk_{\mathrm{Chl}}}, \tag{6.20}$$

where e is the natural exponent.

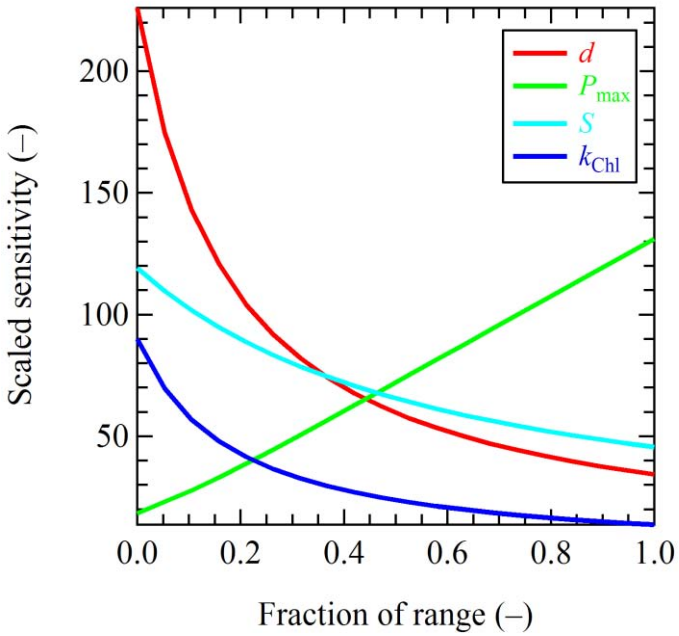

Figure 6.1: Scaled parameter sensitivities.

Now, if an experimentalist has measured d, k_{Chl}, S, and PM for different systems (e.g. different algal strains, different raceway operations, etc.) Equation 6-20 estimates which system is capable of producing the largest biomass concentration.

6.4. Generation of Species Specific Parameters and Constituent Relationships for Potential Production Strains

At the start of this project limited data existed in the literature relating important physiological parameters to algal growth for potential production strains like *N. salina*. Given the diversity of algae growth and productivity even across highly similar species (Sheehan, 1998) it is not acceptable to simply extrapolate from existing literature on related organisms; therefore, a significant undertaking of this project was to generate several relationships for *N. salina*, the strain utilized for our benchtop, greenhouse, and pond-scale experiments.

6.4.1. Generating accurate light extinction coefficients

Light utilization by algae depends on the optical properties of photosynthetic pigment within the cell. While the absorptivity of pigments is generally known in select organic solvents, light extinction is undoubtedly different *in vivo*. Therefore, we developed a quantitative relationship between optical depth (as a function of wavelength) and dry cell weight (DCW) for *N. salina*; thus, generating the absorptivity at all wavelengths. In brief, a dense culture of *N. salina* was used as a stock and serially diluted to create a series of various concentrations of cells. The absorbance of each sample was measured from 300-900 nm and in parallel, the DCW of these same samples were determined gravimetrically. The reference DCW values were projected onto the spectral data using Classical Least Squares to generate the absorptivity curve following Beers' law

$$\varepsilon_\lambda = \frac{A_\lambda}{cl} \tag{6-21}$$

Where ε is the absorptivity at wavelength λ, c is the sample concentration in DCW (μg/ml) and l is the pathlength. Further details to the CLS method is given elsewhere (Haaland, 1985).

The absorbtivity curve that yields the light extinction coefficient, k_B, was measured for *N. salina* grown in the laboratory and used as inoculum for the greenhouse is shown in Figure 6.2. At 680 nm, the light extinction value (used in the model) is $k_B = 0.314$ $(g/m^3)^{-1}/m$.

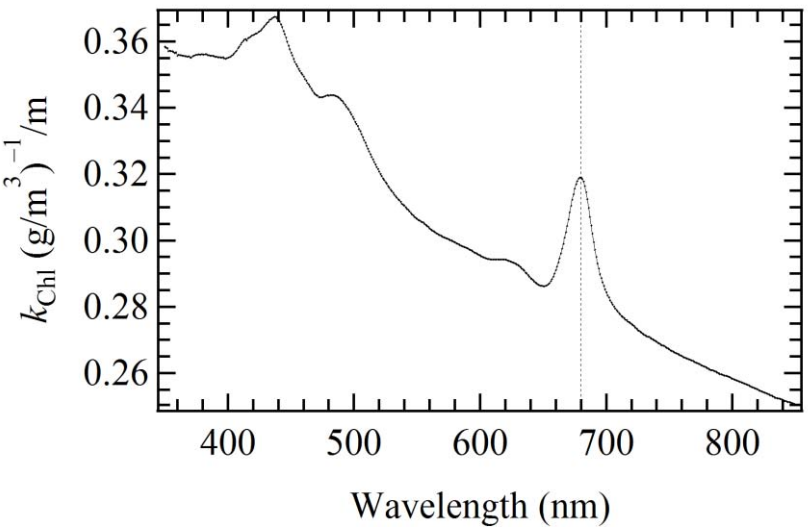

Figure 6.2: Light extinction coefficient measured for laboratory-grown *Nannochloropsis salina* (the 680-nm wavelength is indicated with the dashed line).

6.4.2. Optimal light intensity

Optimal light intensity to grow *N. salina* was also estimated in the laboratory. Low (26 ly/day), medium (35 ly/day), and high (88 ly/day) light intensities were applied to the algae and growth rates measured. While the total biomass at high light intensity was slightly higher than at medium light intensity, the algae grown under the high light intensity were notably less green. The optimal light intensity was specified in the model to be $I_s = 35$ ly/day. Note: 1 Langley/day = 0.48 W/m^2 = 2.3 μmol photosynthetic photons/m^2/s.

6.4.3. Temperature

Reasonable minimum and maximum temperatures for optimal growth of algae in the pond are T_1 = 18°C, and T_2 = 22°C [personal communication from Ann Ruffing, Sandia National Laboratories] and *N. salina*, grows well between 17°C and 32°C (Boussiba, 1987). The minimum and maximum suboptimum temperature-effect coefficients, K_1^T and K_2^T, are 0.693°C^{-2} and 0.007°C^{-2}, respectively, so that at T = 17°C and 32°C, the suboptimal temperature effects restrict algae growth by 50%.

6.4.4. Atomic composition

Algae atomic composition ratios were measured three times over the course of the greenhouse experiment. Samples were collected on days 7, 11, and 14 of the growth experiment yielding C:N:P ratios of 358:38:1, 365:36:1, and 423:39:1, respectively (for reference, the Redfield ratio for marine planktons in open oceans is 106:16:1 (Redfield, 1934)). Significant variability of elemental composition exists across strains and even within strains due to environmental stressors and adaptations. Deviations from this ratio can be used to infer nutrients that limit growth (Hecky, 1993; Hillebrand, 1999; Ricklefs, 2000). Generally, values of N:P less than 16:1 suggest that nitrogen is the limiting nutrient, whereas N:P ratios greater than 16:1 indicate limited phosphorus (Ricklefs, 2000). A C:N:P ratio of 358:38:1 was applied to *N. salina* in the simulation. Initial nitrate and phosphate concentrations were 54.7 and 3.1 g/m^3, respectively. Post-test nitrate was 33.1 g/m^3 and phosphate was below the detection limit after the required dilution.

6.5. Greenhouse Model

The model is also used to simulate algae growth corresponding to an experimental pond maintained inside a greenhouse under known temperature and irradiance conditions. The simulated pond is 1.67×1.5 m^2 and is 0.211 m deep, containing approximately 0.53 m^3 of growth medium. CO_2 is supplied to the system through a bubbler that acts as a point source. While the amount of CO_2 added to the pond was metered, aqueous CO_2 concentrations were not known and some CO_2 certainly escaped to the atmosphere. For the first 7 and last 3 days, air was bubbled at 2 SCFM resulting in 40 g of CO_2 bubbled per day. For the middle 7 days, 2 SCFM of air was augmented with 0.1 SCFM CO_2 (yielding about 5% CO_2). Based on data from (Vance, 2005), 50% of added CO_2 was available to algae when added at a concentration of 0.04% (atmospheric concentration) while only 1% of it was available when added at 5% concentration (i.e., excess CO_2 was assumed lost to the atmosphere). This equated to CO_2 being added at 20 g/day when bubbling air and 80 g/day when bubbling 5% CO_2. Whether or not these CO_2 source rates are appropriate for the greenhouse system is questionable because of atmospheric loss; regardless, CO_2 was never particularly limiting in this model (minimum i(pH) of 0.96).

Algae growth was measured for 17 days after inoculation at 15.4 g/m^3 of biomass. Maximum growth rate at optimum conditions, P_M, was obtained by performing a least squares fit of algal-to-measured biomass using the parameter estimation code, PEST (Doherty, 2009; Doherty, 2010). PEST uses a nonlinear Gauss-Marquardt-Levenberg method to minimize the objective function (i.e., minimize a weighted sum-of-squared differences between the model-generated algae biomass and the measured biomass). A maximum growth rate of P_M = 1.05 day^{-1} was estimated for the greenhouse model (linearized 95% confidence range is 1.01−1.13 day^{-1}). This is consistent with the maximum growth rate of 1.3 day^{-1} reported by Van Wagenen (2012). Recall that the maximum growth rate is mediated by the limitation functions. When considering all of the growth limitations and multiplying by the optimized growth rate of P_M = 1.05 day^{-1}, the maximum production was achieved near day 7 because the product of all limiting factors was greatest and also because 5% CO_2 was added to the system from days 7 to 14. Measured (and modeled) pond productivity was about 1.6 g/m^2/day. Figure 6.3 shows the comparison between the modeled and measured biomass.

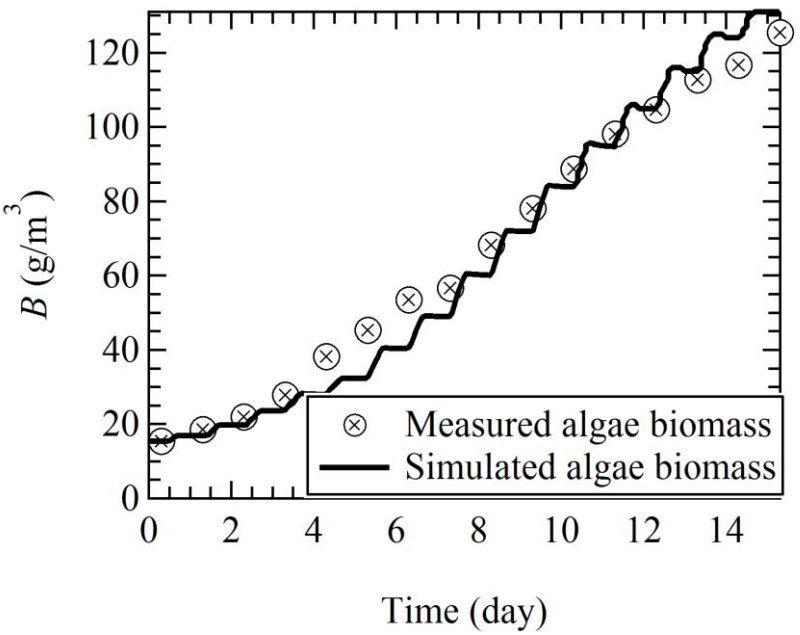

Figure 6.3: Comparison of measured and simulated algal biomasses.

6.6. Conclusions and Future Utility

Models and simulations are quick and inexpensive ways to replicate and extend experiments. SNL-EFDC in conjunction with CE-QUAL was expanded to include the effects of pH and [CO_2] on algae growth as a modeling capability. The improved model was then used to simulate algae growth in an experimental greenhouse pond. Good agreement between estimated and measured algae concentrations was demonstrated when a calibrated maximum growth rate of 1.05 day^{-1} was applied to the model (this was, of course, modulated by limitation factors). These models can now be used with added confidence to predict system behaviors without conducting actual experiments or risking algae colonies. For example, model application to an algae-growth raceway is under development. In the future, this open-source algae growth model, SNL-EFDC, will be improved as new data become available to develop additional empiricisms.

7. CONCLUSIONS

This report describes an integrated multidisciplinary bioanalytical approach for conducting research into the response of algae to abiotic stressors. The approach has been successful across spatial and culture scales and thus has provided new knowledge about the fundamental biological processes that determine algal response and technologies for monitoring and predicting culture behavior. The results have been disseminated through the algal biology and biofuels community through presentations at national and international conferences and through peer-reviewed journal publications. Importantly, the biological insight has prompted new hypothesis that will be the foundation of new proposals as well as validated technology for pond monitoring and computational prediction that will be employed in large-scale algae test-beds in follow-on work.

8. REFERENCES

Adler-Golden SM, Levene RY, Matthew MW, Richtsmeier SC, Bernstein LS, Gruninger J, Felde G, Hoke M, Anderson G, Ratkowski A, Shadow-insensitive material detection/classification with atmospherically corrected hyperspectral imagery. 2001, 4381, 460-469.

Adler-Golden SM, Robertson DC, Richtsmeier SC, Ratkowski A, Cloud effects in hyperspectral imagery from first-principles scene simulations. 2009, 7334, 73340Z.

Affenzeller MJ, Darehshouri A, Andosch A, Lütz C, Lütz-Meindl U, Salt stress-induced cell death in the unicellular green alga Micrasterias denticulata. *Journal of Experimental Botany* 2009; 60(3): 939-954.

Ahn Y-H, Bricaud A, Morel A, Light backscattering efficiency and related properties of some phytoplankters. *Deep Sea Research Part A. Oceanographic Research Papers* 1992; 39(11–12): 1835-1855.

Altschul SF, Gish W, Miller W, Myers EW, Lipman DJ, Basic local alignment search tool. *Journal of Molecular Biology* 1990; 215(3): 403-410.

Apel K, Hirt H, Reactive Oxygen Species: Metabolism, Oxidative Stress, and Signal Transduction. *Annual Review of Plant Biology* 2004; 55(1): 373-399.

Azov Y, Effect of pH on inorganic carbon uptake in algal cultures. *Applied and Environmental Microbiology* 1982; 43(6): 1300-1306.

Badger MR, Andrews TJ, Whitney SM, Ludwig M, Yellowlees DC, Leggat W, Price GD, The diversity and coevolution of Rubisco, plastids, pyrenoids, and chloroplast-based CO2-concentrating mechanisms in algae. *Canadian Journal of Botany* 1998; 76(6): 1052-1071.

Baker KS, Smith RC, Bio-optical classification and model of natural waters. *Limnol. Oceanogr.* 1982; 27: 500-509.

Barbour MM, McDowell NG, Tcherkez G, Bickford CP, Hanson DT, A new measurement technique reveals rapid post-illumination changes in the carbon isotope composition of leaf-respired CO2. *Plant, Cell & Environment* 2007; 30(4): 469-482.

Boussiba S, Vonshak A, Cohen Z, Avissar Y, Richmond A, Lipid and biomass production by the halotolerant microalga *Nannochloropsis salina*. *Biomass* 1987; 12(1): 37-47.

Cerco CF, Cole T, User's Guide to the CE-QUAL-ICM Three-Dimensional Eutrophication Model, Release Version 1.0. U.S. Army Corps of Engineers, 1995.

Clarke A, Desikan R, Hurst RD, Hancock JT, Neill SJ, NO way back: nitric oxide and programmed cell death in Arabidopsis thaliana suspension cultures. *The Plant Journal* 2000; 24(5): 667-677.

Coll NS, Vercammen D, Smidler A, Clover C, Van Breusegem F, Dangl JL, Epple P, Arabidopsis Type I Metacaspases Control Cell Death. *Science* 2010; 330(6009): 1393-1397.

Collins AM, Jones HDT, Han D, Hu Q, Beechem TE, Timlin JA, Carotenoid Distribution in Living Cells of Haematococcus pluvialis (Chlorophyceae). *PLoS ONE* 2011; 6(9): e24302.

Collins AM, Liberton M, Jones HDT, Garcia OF, Pakrasi HB, Timlin JA, Photosynthetic Pigment Localization and Thylakoid Membrane Morphology Are Altered in Synechocystis 6803 Phycobilisome Mutants. *Plant Physiology* 2012; 158(4): 1600-1609.

Craig SE, Lohrenz SE, Lee Z, Mahoney KL, Kirkpatrick GJ, Schofield OM, Steward RG, Use of hyperspectral remote sensing reflectance for detection and assessment of the harmful alga, Karenia brevis. *Appl. Opt.* 2006; 45(21): 5414-5425.

Davis RW, Volponi JV, Jones HDT, Carvalho BJ, Wu H, Singh S, Multiplex fluorometric assessment of nutrient limitation as a strategy for enhanced lipid enrichment and harvesting of Neochloris oleoabundans. *Biotechnology and Bioengineering* 2012; 109(10): 2503-2512.

DeLong JP, Hanson DT, Density-Dependent Individual and Population-Level Metabolic Rates in a Suite of Single-Celled Eukaryotes. *The Open Biology Journal* 2009a; 2: 32-37.

DeLong JP, Hanson DT, Metabolic rate links density to demography in Tetrahymena pyriformis. *ISME J* 2009b; 3(12): 1396-1401.

Doherty JE, Manual for PEST: Model Independent Parameter Estimation. In: Doherty JE, (Ed.). Watermark Numerical Computing, Brisbane, Australia, 2009, pp. 336.

Doherty JE, Addendum to the PEST Manual. In: Doherty JE, (Ed.). Watermark Numerical Computing, Brisbane, Australia, 2010, pp. 131.

Doxaran D, Cherukuru NC, Lavender SJ, Moore GF, Use of a Spectralon Panel to Measure the Downwelling Irradiance Signal: Case Studies and Recommendations. *Appl. Opt.* 2004a; 43(32): 5981-5986.

Doxaran D, Cherukuru RCN, Lavender SJ, Estimation of surface reflection effects on upwelling radiance field measurements in turbid waters. *Journal of Optics A: Pure and Applied Optics* 2004b; 6(7): 690.

Doxaran D, Ruddick K, McKee B, Gentilli D, Tailliez M, Chami M, Babin M, Spectral variations of light scattering by marine particles in coastal waters, from visible to near infrared. *Limnol. Oceanogr.* 2009; 54: 1257-1271.

Gechev TS, Van Breusegem F, Stone JM, Denev I, Laloi C, Reactive oxygen species as signals that modulate plant stress responses and programmed cell death. *BioEssays* 2006; 28(11): 1091-1101.

Genty B, Briantais J-M, Baker NR, The relationship between the quantum yield of photosynthetic electron transport and quenching of chlorophyll fluorescence. *Biochimica et Biophysica Acta (BBA) - General Subjects* 1989; 990(1): 87-92.

Gitelson A, Grits Y, Etzion D, Ning Z, Richmond A, Optical properties of Nannochloropsis sp and their application to remote estimation of cell mass. *Biotechnology and Bioengineering* 2000; 69(5): 516-525.

Goldman JC, Riley CB, Dennett MR, The effect of pH in intensive microalgal cultures. II. Species competition. *Journal of Experimental Marine Biology and Ecology* 1982; 57: 1-13.

Gorman DS, Levine RP, Cytochrome f and plastocyanin: their sequence in the photosynthetic electron transport chain of Chlamydomonas reinhardi. *Proceedings of the National Academy of Sciences* 1965; 54(6): 1665-1669.

Greenberg JT, Programmed Cell Death: A Way of Life for Plants. *PNAS* 1996; 93: 12094-12097.

Haaland DM, Easterling RG, Vopicka DA, Multivariate Least-Squares Methods Applied to the Quantitative Spectral Analysis of Multicomponent Samples. *Applied Spectroscopy* 1985; 39(1): 73-84.

Haaland DM, Jones HDT, Van Benthem MH, Sinclair MB, Melgaard DL, Stork CL, Pedrosa MC, Liu P, Braiser AR, Andrews NL, Lidke DS, Hyperspectral confocal fluorescence imaging: exploring alternative multivariate curve resolution approaches. *Appl. Spectrosc.* 2009; 63: 271-279.

Hansen PJ, Effect of high pH on the growth and survival of marine phytoplankton: Implications for species succession. *Aquatic Microbial Ecology* 2002; 28(3): 279-288.

Hecky RE, Campbell P, Hendzel LL, The stoichiometry of carbon, nitrogen, and phosphorus in particulate matter of lakes and oceans. *Limnol. Oceanogr.* 1993; 38(4): 709-724.

Hillebrand H, Sommer U, The nutrient stoichiometry of benthic microalgal growth: Redfield proportions are optimal. *Limnol. Oceanogr.* 1999; 44(2): 440-446.

Hirata T, Hardman-Mountford N, Aiken J, Fishwick J, Relationship between the distribution function of ocean nadir radiance and inherent optical properties for oceanic waters. *Appl. Opt.* 2009; 48(17): 3129-3138.

Hlaing S, Gilerson A, Harmel T, Tonizzo A, Weidemann A, Arnone R, Ahmed S, Assessment of a bidirectional reflectance distribution correction of above-water and satellite water-leaving radiance in coastal waters. *Appl. Opt.* 2012; 51(2): 220-237.

Hoge FE, Lyon PE, Wright CW, Swift RN, Yungel JK, Chlorophyll biomass in the global oceans: airborne lidar retrieval using fluorescence of both chlorophyll and chromophoric dissolved organic matter. *Appl. Opt.* 2005; 44(14): 2857-2862.

Huertas I, Colman B, Espie G, Mitochondrial-driven bicarbonate transport supports photosynthesis in a marine microalga. *Plant physiology* 2002; 130(1): 284.

Iwasa K, Murakami S, Palmelloid Formation of Chlamydomonas II. Mechanism of Palmelloid Formation by Organic Acids. *Physiologia Plantarum* 1969; 22(1): 43-50.

James SC, Boriah V, Modeling Algae Growth in an Open-Channel Raceway. *Journal of Computational Biology* 2010; 17(7): 895-906.

Janardhanam V, James SC, Sandia National Laboratories Environmental Fluid Dynamics Code: pH Effects User Manual. Sandia National Laboratories, Albuquerque, NM, 2012, pp. 1-22.

Jones HDT, Haaland DM, Sinclair MB, Melgaard DK, Collins AM, Timlin JA, Preprocessing Strategies to Improve MCR Analyses of Hyperspectral Images. *Journal of Chemometrics and Intelligent Laboratory Systems* 2012: in press.

Larkin MA, Blackshields G, Brown NP, Chenna R, McGettigan PA, McWilliam H, Valentin F, Wallace IM, Wilm A, Lopez R, Thompson JD, Gibson TJ, Higgins DG, Clustal W and Clustal X version 2.0. *Bioinformatics* 2007; 23(21): 2947-2948.

Lee Z, Ahn Y-H, Mobley C, Arnone R, Removal of surface-reflected light for the measurement of remote-sensing reflectance from an above-surface platform. *Opt. Express* 2010; 18(25): 26313-26324.

Lee ZP, Du K, Voss KJ, Zibordi G, Lubac B, Arnone R, Weidemann A, An inherent-optical-property-centered approach to correct the angular effects in water-leaving radiance. *Appl. Opt.* 2011; 50(19): 3155-3167.

Livak KJ, Schmittgen TD, Analysis of Relative Gene Expression Data Using Real-Time Quantitative PCR and the $2^{-\Delta\Delta CT}$ Method. *Methods* 2001; 25(4): 402-408.

Mayo AW, Effects of temperature and pH on the kinetic growth of unialga *Chlorella vulgaris* cultures containing bacteria. *Water Environment Research* 1997; 69(1): 64-72.

Merchant SS, Prochnik SE, Vallon O, Harris EH, Karpowicz SJ, Witman GB, Terry A, Salamov A, Fritz-Laylin LK, Marechal-Drouard L, Marshall WF, Qu L-H, Nelson DR, Sanderfoot AA, Spalding MH, Kapitonov VV, Ren Q, Ferris P, Lindquist E, Shapiro H, Lucas SM,

Grimwood J, Schmutz J, Cardol P, Cerutti H, Chanfreau G, Chen C-L, Cognat V, Croft MT, Dent R, Dutcher S, Fernandez E, Fukuzawa H, Gonzalez-Ballester D, Gonzalez-Halphen D, Hallmann A, Hanikenne M, Hippler M, Inwood W, Jabbari K, Kalanon M, Kuras R, Lefebvre PA, Lemaire SD, Lobanov AV, Lohr M, Manuell A, Meier I, Mets L, Mittag M, Mittelmeier T, Moroney JV, Moseley J, Napoli C, Nedelcu AM, Niyogi K, Novoselov SV, Paulsen IT, Pazour G, Purton S, Ral J-P, Riano-Pachon DM, Riekhof W, Rymarquis L, Schroda M, Stern D, Umen J, Willows R, Wilson N, Zimmer SL, Allmer J, Balk J, Bisova K, Chen C-J, Elias M, Gendler K, Hauser C, Lamb MR, Ledford H, Long JC, Minagawa J, Page MD, Pan J, Pootakham W, Roje S, Rose A, Stahlberg E, Terauchi AM, Yang P, Ball S, Bowler C, Dieckmann CL, Gladyshev VN, Green P, Jorgensen R, Mayfield S, Mueller-Roeber B, Rajamani S, Sayre RT, Brokstein P, Dubchak I, Goodstein D, Hornick L, Huang YW, Jhaveri J, Luo Y, Martinez D, Ngau WCA, Otillar B, Poliakov A, Porter A, Szajkowski L, Werner G, Zhou K, Grigoriev IV, Rokhsar DS, Grossman AR, The Chlamydomonas Genome Reveals the Evolution of Key Animal and Plant Functions. *Science* 2007; 318(5848): 245-250.

Moharikar S, D'Souza JS, Kulkarni AB, Rao BJ, APOPTOTIC-LIKE CELL DEATH PATHWAY IS INDUCED IN UNICELLULAR CHLOROPHYTE CHLAMYDOMONAS REINHARDTII (CHLOROPHYCEAE) CELLS FOLLOWING UV IRRADIATION: DETECTION AND FUNCTIONAL ANALYSES1. *Journal of Phycology* 2006; 42(2): 423-433.

Morel A, Gentili B, Diffuse reflectance of oceanic waters. III. Implication of bidirectionality for the remote-sensing problem. *Applied Optics* 1996; 35: 4850-4862.

Moss B, The influence of environmental factors on the distribution of freshwater algae: An experimental study: II. The roles of pH and the carbondioxide-bicarbonate system. *Journal of Ecology* 1973; 61(1): 157-177.

Park PK, Oceanic CO_2 system: An evaluation of ten methods of investigation. *Limnol. Oceanogr.* 1969; XIV(2): 179-186.

Pedroso MC, Sinclair MB, Jones HDT, Haaland DM, Hyperspectral Confocal Fluorescence Microscope: A New Look into the Cell. *Microscopy Today* 2010; 18(05): 14-18.

Porra RJ, Thompson WA, Kriedemann PE, Determination of accurate extinction coefficients and simultaneous equations for assaying chlorophylls a and b extracted with four different solvents: verification of the concentration of chlorophyll standards by atomic absorption spectroscopy. *Biochimica et Biophysica Acta (BBA) - Bioenergetics* 1989; 975(3): 384-394.

Quirantes A, Bernard S, Light-scattering methods for modeling algal particles as a collection of coated and/or nonspherical scatterers. *J. Quant. Spectrosc. & Rad. Trans.* 2006; 100: 315-324.

Raven JA, Nutrient transport in microalgae. *Advances in Microbail Physiology* 1980; 21: 47-226.

Redfield AC, On the proportions of organic derivatives in sea water and their relation to the composition of plankton. In *James Johnstone Memorial Volume*. Daniel RJ, (Ed.), University Press of Liverpool, London, 1934, pp. 176-192.

Reichardt TA, Collins AM, Garcia OF, Ruffing AM, Jones HDT, Timlin JA, Spectroradiometric Monitoring of Nannochloropsis salina Growth. *Algal Research* 2012; 1(1): 22-31.

Ricklefs RE, Miller GL, Ecology. Macmillan, New York 2000.

Ruffing AM, Jones HDT, Physiological effects of free fatty acid production in genetically engineered Synechococcus elongatus PCC 7942. *Biotechnology and Bioengineering* 2012; 109(9): 2190-2199.

Sharkey T, Berry J, Carbon isotope fractionation of algae as influenced by an inducible CO2 concentrating mechanism. *Inorganic carbon uptake by aquatic photosynthetic organisms. American Society of Plant Physiologists* 1985: 389–401.

Sheehan J, Dunahay T, Benemann J, Roessler P, A Look Back at the U.S. Department of Energy's Aquatic Species Program: Biodiesel from Algae. 1998.

Sinclair MB, Haaland DM, Timlin JA, Jones HDT, Hyperspectral confocal microscope. *Applied Optics* 2006; 45(24): 3283-3291.

Singh NK, Bajwa SG, Chaubey I, Removal of Surface Reflection from Above-Water VisibleNear Infrared Spectroscopic Measurements. *Applied Spectroscopy* 2008; 62(9): 1013-1021.

Smith AF, Raven JA, Intracellular pH and its regulation. *Annual Review of Plant Physiology* 1979; 30: 289-311.

Stern D, Witman GB, The Chlamydomonas Sourcebook: Introduction to Chlamydomonas and Its Laboratory Use. Academic Press, 2008.

Stramski D, Bricaud A, Morel A, Modeling the Inherent Optical Properties of the Ocean Based on the Detailed Composition of the Planktonic Community. *Appl. Opt.* 2001; 40(18): 2929-2945.

Svensen Ø, Frette Ø, Erga SR, Scattering properties of microalgae: the effect of cell size and cell wall. *Appl. Opt.* 2007; 46(23): 5762-5769.

Thanh PHX, Grace MD, James SC, Sandia National Laboratories Environmental Fluid Dynamics Code: Sediment Transport User Manual. Sandia National Laboratories, Albuquerque, NM, 2008, pp. 1-47.

Timlin JA, Sinclair MB, Haaland DM, Aragon AD, Martinez MJ, Werner-Washburne M, Hyperspectral microarray scanning: Impact on the accuracy and reliability of gene expression data. *BMC Genomics* 2005; 6(72).

Tsiatsiani L, Van Breusegem F, Gallois P, Zavialov A, Lam E, Bozhkov PV, Metacaspases. *Cell Death Differ* 2011; 18(8): 1279-1288.

Vaillancourt RD, Brown CW, Guillard RRL, Balch WM, Light backscattering properties of marine phytoplankton: relationships to cell size, chemical composition and taxonomy. *Journal of Plankton Research* 2004; 26(2): 191-212.

Van Wagenen J, Miller TW, Hobbs S, Hook P, Crowe B, Huesemann M, Effects of light and temperature on fatty acid production in *Nannochloropsis Salina*. *Energies* 2012; 5(3): 731-740.

Vance P, Spalding M, Growth, photosynthesis, and gene expression in Chlamydomonas over a range of CO2 concentrations and CO2/O2 ratios: CO2 regulates multiple acclimation states. *Canadian Journal of Botany* 2005; 83(7): 796-809.

Vermaas WFJ, Timlin JA, Jones HDT, Sinclair MB, Nieman LT, Hamad SW, Melgaard DK, Haaland DM, In vivo hyperspectral confocal fluorescence imaging to determine pigment localization and distribution in cyanobacterial cells. *Proceedings of the National Academy of Sciences* 2008; 105(10): 4050.

Whitmire AL, Pegau WS, Karp-Boss L, Boss E, Cowles TJ, Spectral backscattering properties of marine phytoplankton cultures. *Opt. Express* 2010; 18(14): 15073-15093.

Zhou W, Wang G, Sun Z, Cao W, Xu Z, Hu S, Zhao J, Variations in the optical scattering properties of phytoplankton cultures. *Opt. Express* 2012; 20(10): 11189-11206.

Zibordi G, Berthon J-F, Relationships between Q-factor and seawater optical properties in a coastal region. *Limnol. Oceanogr.* 2001; 46: 1130-1140.

APPENDIX A: PRIMERS USED IN REAL-TIMEQUANTTITAVE PCR ASSAYS

Joint Genome Institute Accession Numbers	Gene Name	Pfam	KOG	Gene Ontology Terms	Primer Orientation (with respect to the Watson strand)	Primer Sequence	Genome Coordinates	In House Primer name
Cre02.g108400	DAD1	Pfam:02109 DAD family	KOG:1746 Defender against cell death protein/oligosaccharyltransferase, epsilon subunit	GO:0016021 integral to membrane	Forward	ACT CCA GTC CGT GTG AAG GTT	Chromosome 2: 4,618,091-4,618,110	Dad1F2
Cre02.g108400	DAD1	Pfam:02109 DAD family	KOG:1746 Defender against cell death protein/oligosaccharyltransferase, epsilon subunit		Reverse	GGC AGT AGT CGC CGA AGG C	Chromosome 2: 4,618,796-4,618,778	Dad1R2
Cre12.g517450	Metacaspase 1	Pfam:00656 Caspase domain	KOG:1546 Metacaspase involved in regulation of apoptosis	GO:0004197 cysteine-type endopeptidase activity; GO:0006508 proteolysis and peptidolysis	Forward	ACC AGC AGC CCG GTG ACT C	Chromosome 12: 3,912,205-3,912,223	Mcasp1 F5
Cre12.g517450	Metacaspase 1	Pfam:00656 Caspase domain	KOG:1546 Metacaspase involved in regulation of apoptosis		Reverse	CGC GGT AGG GAA GGT CCA G	Chromosome 12: 3,911,796-3,911,778	Mcasp1 R5
Cre01.g042750	Aconitate hydratase	Pfam:00694 Aconitase C-terminal domain; Pfam:00330 Aconitase family (aconitate hydratase)	KOG:0453 Aconitase/homoaconitase (aconitase superfamily)	GO:0008152 metabolism	Forward	GTG GCG ATG CAG GAC GCG ACT G	Chromosome 1: 5,890,462-5,890,483	Aconitase F
Cre01.g042750	Aconitate hydratase	Pfam:00694 Aconitase C-terminal domain; Pfam:00330 Aconitase family (aconitate hydratase)	KOG:0453 Aconitase/homoaconitase (aconitase superfamily)	GO:0008152 metabolism	Reverse	GGA GGT GTA CGA CTT CCT GGC TAC	Chromosome 1: 5,890,850-5,890,827	Aconitase R
Cre02.g092000	DEG2; DegP-type protease	Pfam:00089 Trypsin	KOG:1320 Serine protease	GO:0004252 serine-type endopeptidase activity; GO:0006508 proteolysis and peptidolysis	Forward	GAT GGC GCA GAG CAA GTC CAC CG	Chromosome 2: 2,371,085-2,371,107	DegP F
Cre02.g092000	DEG2; DegP-type protease	Pfam:00089 Trypsin	KOG:1320 Serine protease	GO:0004252 serine-type endopeptidase activity; GO:0006508 proteolysis and peptidolysis	Reverse	CCA TGC TGA CCG TGG ACA ACG ACG	Chromosome 2: 2,370,931-2,370,908	DegP R
Cre08.g372100	Heat shock protein; Heat shock protein 70A	Pfam:00012 Hsp70 protein	KOG:0100 Molecular chaperones GRP78/BiP/KAR2, HSP70 superfamily		Forward	GTG GCC TTC ACG GAC ACT GAG CG	Chromosome 8: 2,075,672-2,075,694	HSP70-295F
Cre08.g372100	Heat shock protein; Heat shock protein 70A	Pfam:00012 Hsp70 protein	KOG:0100 Molecular chaperones GRP78/BiP/KAR2, HSP70 superfamily		Reverse	GCT GTG GCC TTT CCA GGT TCG CG	Chromosome 8: 2,075,479-2,075,457	HSP70-532R

Distribution (all copies electronic)

1 David T. Hanson
Department of Biology
University of New Mexico
Albuquerque, New Mexico 87131

2 Thomas A. Dempster, John McGowen
Arizona Center for Technology and Innovation
Arizona State University
Mesa, AZ 85212

1	MS0754	Brian P. Dwyer	06912
1	MS0895	Jerilyn A. Timlin	08622
1	MS0895	Howland D.T. Jones	08622
1	MS1163	Omar F. Garcia	05448
1	MS1413	Aaron. M. Collins	08622
1	MS1413	Anne Ruffing	08622
1	MS1413	Kylea Parchert	08622
1	MS1413	Christine Trahan	08622
1	MS1413	James Carney	08622
1	MS1413	Amy J. Powell	08635
1	MS9056	Thomas A. Reichardt	08128
1	MS9292	Benjamin Wu	08634
1	MS9409	Patricia E. Gharagozloo	08365
1	MS9409	Gregory Wagner	08365

1	MS0899	Technical Library	9536
1	MS0359	D. Chavez, LDRD Office	1911


Sandia National Laboratories